LIVERPOOL JOHN MOORES UNIVERSITY

LJMU Research Online

Green, AW, Glazebrook, K, McGregor, PJ, Damjanov, I, Wisnioski, E, Abraham, RG, Colless, M, Sharp, RG, Crain, RA, Poole, GB and McCarthy, PJ

DYNAMO - I. A sample of H alpha-luminous galaxies with resolved kinematics

http://researchonline.ljmu.ac.uk/id/eprint/4696/

Article

Citation (please note it is advisable to refer to the publisher's version if you intend to cite from this work)

Green, AW, Glazebrook, K, McGregor, PJ, Damjanov, I, Wisnioski, E, Abraham, RG, Colless, M, Sharp, RG, Crain, RA, Poole, GB and McCarthy, PJ (2014) DYNAMO - I. A sample of H alpha-luminous galaxies with resolved kinematics. Monthly Notices of the Royal Astronomical Society, 437 (2), pp.

LJMU has developed **LJMU Research Online** for users to access the research output of the University more effectively. Copyright © and Moral Rights for the papers on this site are retained by the individual authors and/or other copyright owners. Users may download and/or print one copy of any article(s) in LJMU Research Online to facilitate their private study or for non-commercial research. You may not engage in further distribution of the material or use it for any profit-making activities or any commercial gain.

The version presented here may differ from the published version or from the version of the record. Please see the repository URL above for details on accessing the published version and note that access may require a subscription.

For more information please contact researchonline@ljmu.ac.uk

http://researchonline.ljmu.ac.uk/

Monthly Notices
of the
ROYAL ASTRONOMICAL SOCIETY

MNRAS **437,** 1070–1095 (2014)
Advance Access publication 2013 November 14

doi:10.1093/mnras/stt1882

DYNAMO – I. A sample of Hα-luminous galaxies with resolved kinematics

Andrew W. Green,[1⋆] Karl Glazebrook,[2] Peter J. McGregor,[3] Ivana Damjanov,[4] Emily Wisnioski,[5] Roberto G. Abraham,[6] Matthew Colless,[3] Robert G. Sharp,[3] Robert A. Crain,[7] Gregory B. Poole[8] and Patrick J. McCarthy[9,10]

[1]*Australian Astronomical Observatory, PO Box 970, North Ryde, NSW 1670, Australia*
[2]*Centre for Astrophysics and Supercomputing, Swinburne University, Hawthorn VIC 3122, Australia*
[3]*Research School of Astronomy and Astrophysics, Australian National University, Cotter Rd, Weston, ACT 2611, Australia*
[4]*Harvard-Smithsonian CfA, 60 Garden St., MS-20, Cambridge, MA 02138, USA*
[5]*Max-Plank-Institut für extraterrestrische Physik, Postfach 1312, Giessenbachstr., D-85741 Garching, Germany*
[6]*Department of Astronomy and Astrophysics, University of Toronto, 50 St George St., Toronto, ON M5S3H4, Canada*
[7]*Leiden Observatory, PO Box 9513, NL-2300 RA Leiden, the Netherlands*
[8]*School of Physics, The University of Melbourne, Parkville VIC 3010, Australia*
[9]*Observatories of the Carnegie Institution of Washington, 813 Santa Barbara Street, Pasadena, CA 91101, USA*
[10]*Giant Magellan Telescope Organization, 251 S. Lake Avenue, Suite 300, Pasadena, CA 91101, USA*

Accepted 2013 October 2. Received 2013 October 2; in original form 2013 July 23

ABSTRACT

DYNAMO is a multiwavelength, spatially resolved survey of local ($z \sim 0.1$) star-forming galaxies designed to study evolution through comparison with samples at $z \simeq 2$. Half of the sample has integrated Hα luminosities of $>10^{42}$ erg s^{-1}, the typical lower limit for resolved spectroscopy at $z \simeq 2$. The sample covers a range in stellar mass (10^9–10^{11} M$_\odot$) and star formation rate (0.2–100 M$_\odot$ yr^{-1}). In this first paper of a series, we present integral-field spectroscopy of Hα emission for the sample of 67 galaxies. We infer gas fractions in our sample as high as ≃0.8, higher than typical for local galaxies. Gas fraction correlates with stellar mass in galaxies with star formation rates below 10 M$_\odot$ yr^{-1}, as found by COLDGASS, but galaxies with higher star formation rates have higher than expected gas fractions. There is only a weak correlation, if any, between gas fraction and gas velocity dispersion. Galaxies in the sample visually classified as disc-like are offset from the local stellar mass Tully–Fisher relation to higher circular velocities, but this offset vanishes when both gas and stars are included in the baryonic Tully–Fisher relation. The mean gas velocity dispersion of the sample is $\simeq 50$ km s^{-1}, and V/σ ranges from 2 to 10 for most of the discs, similar to 'turbulent' galaxies at high redshift. Half of our sample show disc-like rotation, while ∼20 per cent show no signs of rotation. The division between rotating and non-rotating is approximately equal for the sub-samples with either star formation rates >10 M$_\odot$ yr^{-1}, or specific star formation rates typical of the star formation 'main sequence' at $z \simeq 2$. Across our whole sample, we find good correlation between the dominance of 'turbulence' in galaxy discs (as expressed by V/σ) and gas fraction as has been predicted for marginally stable Toomre discs. Comparing our sample with many others at low- and high-redshift reveals a correlation between gas velocity dispersion and star formation rate. These findings suggest the DYNAMO discs are excellent candidates for local galaxies similar to turbulent $z \simeq 2$ disc galaxies.

Key words: galaxies: evolution – galaxies: formation – galaxies: kinematics and dynamics – galaxies: star formation.

1 INTRODUCTION

At high redshift, galaxies have much higher star formation rates (SFR) than galaxies today (Madau et al. 1996; Hopkins & Beacom 2006). Massive galaxies in particular are very strongly star

⋆ E-mail: andrew.green@aao.gov.au

© 2013 The Authors
Published by Oxford University Press on behalf of the Royal Astronomical Society

Downloaded from http://mnras.oxfordjournals.org/ at Liverpool John Moores University on October 27, 2016

forming, unlike their modern counterparts (Bell et al. 2005; Juneau et al. 2005). It has long been known that star-forming galaxies at high redshift also exhibit very different physical morphologies from the local Hubble sequence, and a large number have a clumpy and irregular morphology (Abraham et al. 1996a,b; van den Bergh et al. 1996; Conselice 2003). Such structures could be associated with merging objects and early modelling suggested that such merging would be the primary mechanism of mass growth of massive galaxies (Baugh, Cole & Frenk 1996; Cole et al. 2000). More recently, clumpy morphologies have been viewed as clumpy star formation patterns in disc galaxies (Noguchi 1998; Elmegreen, Elmegreen & Hirst 2004; Elmegreen & Elmegreen 2005, 2006; Genzel et al. 2006, 2011; Bournaud, Elmegreen & Martig 2009; Elmegreen et al. 2009) with the growth of mass dominated by in situ star formation from cosmological accretion (Dekel, Sari & Ceverino 2009; Dekel et al. 2009; Ceverino, Dekel & Bournaud 2010). Kinematic studies offer the possibility to distinguish clumpy discs from mergers.

Scenarios that explain the differences seen in high-redshift galaxies have been tested with spatially resolved kinematics, primarily probing the strong Hα emission line associated with star formation (see Glazebrook 2013, for a review). In the clumpy disc picture, galaxies may be photometrically irregular but kinematically regular, and numerous examples have now been observed (Erb et al. 2006b; Genzel et al. 2006, 2011; Wright et al. 2007; Förster Schreiber et al. 2009; Wisnioski et al. 2011). A fraction of 30–50 per cent of massive galaxies at $z > 1$ may be discs, with the fraction likely increasing with stellar mass (Förster Schreiber et al. 2009; Law et al. 2009). Despite the demonstrated existence of disc galaxies, the observed merger rate is also high, with typically 30–50 per cent of galaxies in integral-field spectroscopic surveys demonstrating merger-like kinematics (Yang et al. 2008; Förster Schreiber et al. 2009; Vergani et al. 2012).

The rotation velocities, V, of disc galaxies at high redshift are similar to those of local galaxies, with little or no evolution in the Tully–Fisher relation (TFR) at fixed stellar mass (Kassin et al. 2007; Cresci et al. 2009; Puech et al. 2010; Gnerucci et al. 2011; Miller et al. 2011; Vergani et al. 2012). An unexpected finding was the high velocity dispersion, σ, of many high-redshift discs. Values of 50–100 km s^{-1} (Genzel et al. 2006; Law et al. 2007a, 2009; Förster Schreiber et al. 2009; Gnerucci et al. 2011; Vergani et al. 2012) are regularly observed. With typical ratios $V/\sigma \sim$ 1–5, such discs are dynamically much 'hotter' than local spiral discs where $V/\sigma \sim$ 10–20 (Andersen et al. 2006; Epinat et al. 2010). This difference has been attributed to high fractions (by mass) of gas (Genzel et al. 2011). Such high fractions of gas have been observed (Daddi et al. 2010; Tacconi et al. 2010, 2013; Carilli & Walter 2013) and in some cases resolved molecular gas observations have confirmed the high-dispersion discs seen in Hα (Swinbank et al. 2011; Hodge et al. 2012).

Also at high redshift, a significant population of 'dispersion-dominated' galaxies with $\sigma \gtrsim V$ and stellar masses $>10^{10}$ M$_\odot$ has been identified (Law et al. 2007a, 2009). Dispersion-dominated galaxies of this mass only appear above $z \gtrsim 1$ (Kassin et al. 2012). These are generally quite compact (half-light radii <2 kpc) and may be unresolved small discs (Newman et al. 2013).

High velocity dispersion seems to be a universal feature of galaxies at high redshift. The velocity dispersions are supersonic and likely represent a highly turbulent interstellar medium. A large turbulent velocity dispersion and pressure support gives rise to a large Jeans mass (10^8–10^9 M$_\odot$; see Elmegreen et al. 2009) for gravitational collapse and hence imply that galactic star formation will be dominated by a handful of giant clumps, consistent with the irregular morphologies. The physical mechanism sustaining the turbulence, which would otherwise decay quickly, is not yet determined but may be due to star formation feedback (Lehnert et al. 2009, 2013; Green et al. 2010; Le Tiran et al. 2011), initial gravitational collapse (Elmegreen & Burkert 2010), ongoing cosmic accretion (Aumer et al. 2010), gravitational instabilities (Immeli et al. 2004; Bournaud et al. 2010; Ceverino et al. 2010; Aumer et al. 2010) or some combination thereof.

It is important to note that integral-field spectroscopy at high redshift is intrinsically difficult and is subject to selection effects, resolution and surface-brightness limitations. The technique of adaptive optics (AO; reviewed by Davies & Kasper 2012) has allowed observations at ∼0.1 arcsec resolution (0.8 kpc for $1 < z < 3$). However, these observations are possible only in a limited number of cases due to guide star and other constraints; the largest AO samples number 10–35 objects (Law et al. 2009; Wisnioski et al. 2011; Newman et al. 2013). Techniques using AO only correct a fraction of the light into a compact point spread function (PSF) and necessitate finer detector sampling; hence the observations are only sensitive to features with the highest surface brightness. Nonetheless, they are essential for resolved spectroscopic studies of galaxy sub-structures such as clumps. Techniques using AO have also been enhanced in many cases by the gravitational lensing of giant clusters of galaxies, delivering 200–300 pc resolution and probing sub-luminous galaxies (Nesvadba et al. 2006, 2007; Swinbank et al. 2007, 2009; Stark et al. 2008; Jones et al. 2010; Yuan et al. 2011, 2012), albeit with highly anamorphic magnification.

The majority of integral-field spectroscopy at high redshift has been performed *without* the resolution improvements provided by AO. Whilst 'natural seeing' observations have fewer complications, they only offer 5–8 kpc resolution. Since the point-spread function is comparable to the size of the galaxies studied, astronomers must rely to a much greater extent on model fitting to describe each galaxy's physical parameters (Cresci et al. 2009; Lemoine-Busserolle & Lamareille 2010; Epinat et al. 2012). The models used include many assumptions about the real physical structure of the galaxies to which they are applied. With or without AO, instrument sensitivity limits most integral-field spectroscopic surveys to high-redshift galaxies with Hα luminosities of $>10^{42}$ erg s^{-1} (e.g. Förster Schreiber et al. 2009; Law et al. 2009; Wright et al. 2009). Although only a few per cent of local galaxies reach this luminosity, it does correspond to 'normal' galaxies at $z \sim 2$ in that they follow the SFR–stellar mass 'main sequence' (Daddi et al. 2007; Noeske et al. 2007).

Integral-field spectroscopic data of local galaxies comparable to existing high-redshift samples can clarify the interpretation of high-redshift-galaxy data. A sample of low-redshift galaxies would allow the methods applied to high-redshift galaxies to be tested on data with higher signal-to-noise-ratio and higher resolution (e.g., fitting 2D disc models or testing for mergers with kinemetry as in Shapiro et al. 2008), and on artificially redshifted data (where the appearance of a galaxy at high redshift is simulated with all the noise, PSF, resolution and sensitivity effects included). Until recently, integral-field spectroscopy of local galaxies has not been widely available, as historical work has relied on long-slit spectroscopy. However, surveys such as ATLAS^{3D} (Cappellari et al. 2011), GHASP (Epinat et al. 2010), CALIFA (Sánchez et al. 2012) and DISKMASS (Bershady et al. 2010) have now provided integral-field spectroscopy of well-resolved, large and local galaxies (within ∼100 mpc and as large as ∼ 1 arcmin on the sky). None of these samples includes galaxies with SFR comparable to $z \sim 2$ objects.

Downloaded from http://mnras.oxfordjournals.org/ at Liverpool John Moores University on October 27, 2016

It is desirable to construct such a sample to allow the effects of SFR and temporal evolution to be considered separately, for example.

There are several samples of local luminous and ultraluminous infrared galaxies (LIRGs/ULIRGs) observed with integral-field spectroscopy that can be used for comparison with high-redshift samples. Colina, Arribas & Monreal-Ibero (2005) compared the stellar kinematics with the ionized- and molecular-gas kinematics of 11 ULIRGs in order to gain insight into similar measurements of $z \simeq 2$ galaxies. Arribas et al. (2008) have observed 42 (U)LIRGs selected by their far-infrared emission. More recently, Arribas et al. (2012) and Westmoquette et al. (2012) have furthered the comparisons with larger and more detailed samples, and applied many of the analysis popularly employed for high-redshift samples to the local ULIRGs, respectively. These samples of ULIRGs have greatly expanded our understanding of highly star-forming galaxies in the nearby Universe.

In addition to selections based on infrared luminosity, there is also integral-field spectroscopy of galaxy samples selected on ultraviolet luminosity. Basu-Zych et al. (2009) and Gonçalves et al. (2010) obtained AO-corrected, integral-field spectroscopic data of 19 galaxies at $z \sim 0.2$. These galaxies were selected via near-ultraviolet emission to be analogous to $z \sim 3$ 'Lyman-break Galaxy' dropout selections (Steidel et al. 1996) and selected to have compact morphologies with high surface brightnesses. Interestingly infrared- and ultraviolet-selected samples include some galaxies that are clearly mergers, but could be misclassified as discs in simulated $z \sim 2$ observations (Gonçalves et al. 2010; Bellocchi, Arribas & Colina 2012). The 'Lyman-break analogues' show only weak velocity shears ($V/\sigma \sim 1$) and could be similar to high-redshift, dispersion-dominated galaxies. Neither sample probes large, rotationally dominated galaxies with high stellar mass.

In this paper, we present integral-field spectroscopy of a new sample of nearby galaxies selected to have high SFR. We select our sample primarily by Hα luminosity in order to maximize the physical overlap with high-redshift galaxies. The spatial resolution of our data (1–3 kpc) is comparable to high-redshift samples observed with AO. This paper provides the core description of the survey and some initial scientific results. We also expand on the early results on the relation of star formation and velocity dispersion presented in Green et al. (2010) and make a case that a number of these galaxies are rotationally supported turbulent discs. Later papers in the series will delve more deeply into other physical comparisons.

The plan of this paper is as follows. We begin in Section G2 by describing the sample in detail, including the selection criteria, properties of the sample and some of the sample selection biases. Section 3 presents the optical integral-field spectroscopy of these galaxies, and describes the removal of the instrumental signature from the data. The data analysis methods are described in Section 4. Results from these data are presented in Section 5, including SFR (Section 5.2), estimates of gas content (Section 5.3) and the TFR (Section 5.4). The relationship between galaxy SFR and gas turbulence which was highlighted in Green et al. (2010) is expanded in Section 5.6. We discuss our results and outline the plan for this series of papers in Section 6. Section 7 summarizes our conclusions.

Throughout this paper, we will use the cosmology given by $H_0 = 71\,\mathrm{km\,s^{-1}\,Mpc^{-1}}$, $\Omega_\mathrm{M} = 0.27$ and $\Omega_\lambda = 0.73$. We use a Chabrier (2003) initial mass function (IMF). For conversions from other IMFs, we adopt the following mass ratios: Salpeter – 1/1.8 (Erb et al. 2006a), Kroupa 2001 – 1/0.88 (Lemoine-Busserolle et al. 2010) and diet Salpeter – 1/1.19 (Cresci et al. 2009).

2 THE DYNAMO SAMPLE

2.1 Sample selection

We have selected a representative sample of 67 galaxies classified as star forming in the Max-Planck-Institut für Astrophysik and Johns Hopkins University (MPA-JHU) value-added catalogue[1] of the Sloan Digital Sky Survey (SDSS, York et al. 2000). This value-added catalogue provides stellar masses, metallicities and SFR, which are based on improved fits to the original SDSS spectra (Kauffmann et al. 2003a; Brinchmann et al. 2004; Tremonti et al. 2004). Our sample has been designed to include the most highly Hα-luminous, star-forming galaxies, as well as lower Hα-luminosity galaxies more common in the local Universe.

The sample galaxies were selected by redshift and Hα emission flux or luminosity as measured in the SDSS 3.0 arcsec-diameter fibre aperture. Galaxies have been selected principally in two redshift (z) ranges that avoid placing their Hα emission on significant night-sky emission and absorption features; $0.055 < z < 0.084$ and $0.129 < z < 0.151$. Within these redshift constraints, a series of selection windows in flux or luminosity of the Hα emission line were defined. Five-to-ten galaxies were chosen within each window. To include rarer galaxies with high Hα luminosities, the redshift constraint was relaxed to $z < 0.154$ or $0.174 < z < 0.3$, which avoids only the most significant telluric absorption feature. Thus, equal numbers of both rare and more common galaxies were selected, despite significant change in the underlying number density with luminosity. Each window is identified by a letter (A through I) in Fig. 1. Although galaxies were selected in window I, none have been observed for this paper, but will ultimately be included in the DYNAMO sample. The criteria for the selection windows and the number of galaxies in each window are shown in Table 1. Fig. 1 shows the selection windows and locations of the selected galaxies, as well as the distribution of SDSS star-forming galaxies from Brinchmann et al. (2004).

We target the Hα emission line specifically because it is both easily detected, and makes a good probe of star formation and gas kinematics. One of our primary goals is to compare our sample with galaxy samples at high redshift. Where possible, most high-redshift integral-field spectroscopy uses the same Hα emission line for the same reasons. For $z \simeq 2$ galaxies, the typical detection limit in one hour using integral-field spectroscopy corresponds to an SFR of $1\,\mathrm{M_\odot\,yr^{-1}\,kpc^{-2}}$, even on 8–10 m telescopes (Law et al. 2007b). Consequently, high-redshift samples are often effectively limited to Hα luminosities of at least $10^{42}\,\mathrm{erg\,s^{-1}}$ by the observed flux of the emission line, independent of other criteria.[2] At lower redshift, this limitation is alleviated, so lower luminosity galaxies can be detected with integral-field spectroscopy. The SDSS fibre typically does not sample all of the Hα emission from a galaxy. We will show in Section 4.2 that galaxies with Hα luminosities within the SDSS fibre of $10^{41.27}\,\mathrm{erg\,s^{-1}}$ have total Hα luminosities representing the typical high-redshift limit, so our sample overlaps samples at high redshift.

The galaxies of our sample are listed in Table 3, including the window from which they were selected and their SDSS designation. Table 4 lists the redshift of the galaxy from the SDSS DR4 data base (Adelman-McCarthy et al. 2006). The stellar masses, $\mathcal{M}_*$, of our galaxies range from 1.09 to $65.0 \times 10^9\,\mathrm{M_\odot}$ after IMF correction

[1] http://www.mpa-garching.mpg.de/SDSS/DR4/

[2] For example, see fig. 1 of Wisnioski et al. (2011) for a graphical illustration of this.

Downloaded from http://mnras.oxfordjournals.org/ at Liverpool John Moores University on October 27, 2016

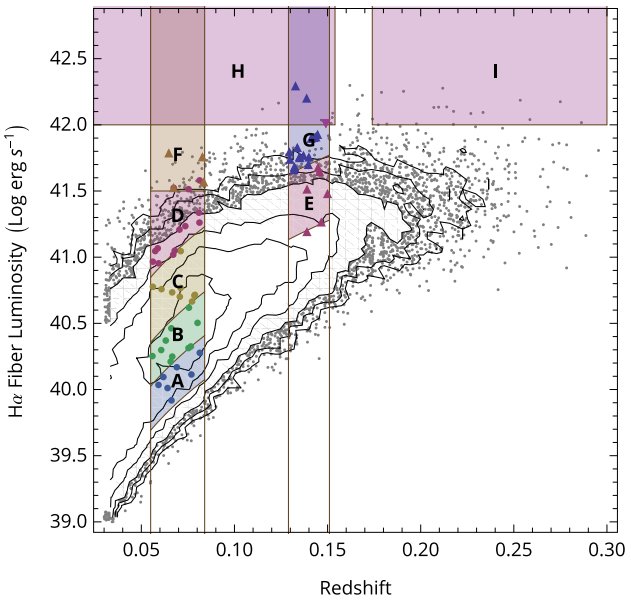

Figure 1. Target selection windows in Hα luminosity (measured within the 3 arcsec SDSS fibre aperture) and redshift. The population of all star-forming (classified as ' SF' by Brinchmann et al. 2004) galaxies in SDSS is shown by the small grey points and the logarithmic density contours. Galaxies making up the sample here were randomly selected from this population inside each shaded window, and are shown with coloured points and shapes corresponding to the selection window. Note that the selection windows for regions F and G overlap with that for H. Regions A, B, C, D, E and G have curved limits because they are flux-limited regions instead of luminosity-limited regions.

Table 1. Target categories.

Categories	Selection criteria z	Hα[a]	$n_{\rm selected}$
A	$0.055 < z < 0.084$	$65 < f < 140$	7
B	$0.055 < z < 0.084$	$140 < f < 300$	10
C	$0.055 < z < 0.084$	$300 < f < 930$	9
D	$0.055 < z < 0.084$	$930 < f$	13
E	$0.129 < z < 0.151$	$300 < f < 930$	6
F	$0.055 < z < 0.084$	$41.5 < L$	7
G	$0.129 < z < 0.151$	$930 < f$	17
H	$z < 0.154$	$42.0 < L$	1
I	$0.174 < z$	$42.0 < L$	0[b]
Total			67

[a]For a galaxy to be selected, its Hα emission was required to meet either a flux range or a luminosity range in the MPA-JHU value-added catalogue measurements of SDSS spectra. Flux requirements are denoted by f and have units of 10^{-17} erg s^{-1} cm^{-2}, while luminosity requirements are denoted by L and have units of log erg s^{-1}.
[b]Although galaxies were selected in window I, none of them has been observed at the time of writing. Window I is included for completeness in subsequent papers of this series.

(Kauffmann et al. 2003a). The stellar masses, as well as Hα luminosities measured within the fibre, [$L_{\rm fibre}$(Hα), from Tremonti et al. 2004], and aperture-corrected SFR (SFR$_{\rm B04}$, from Brinchmann et al. 2004) are also listed in Table 4.

Fig. 2 shows the colour–mass diagram for the two main redshift bands of the sample. SDSS $u - r$ colour separates the red sequence of galaxies from the blue cloud (Baldry et al. 2004, 2006). Each panel shows the $u - r$ colour and stellar masses for all SDSS galaxies (not just those that are star forming) that meet the corresponding redshift requirement. The galaxies of our sample have been highlighted within each redshift range. For the lower-redshift range, the sample is representative of the blue cloud, but in the higher redshift range only fairly extreme blue galaxies are included. The effect of the SDSS apparent magnitude limit for spectroscopy is also noticeable, as only more massive galaxies are included in the higher redshift range. Overall, the sample is fairly representative of the blue cloud at $z \sim 0.1$.

Our sample can be compared with samples of galaxies observed with integral-field spectroscopy at high redshift in three different ways. First, galaxies in our sample with Hα luminosities above 10^{42} erg s^{-1} can be directly compared with similarly luminous galaxies at high redshift. In this way, galaxies with similar SFR in different eras can be compared as a probe of the physical processes regulating star formation. Secondly, a comparison of the DYNAMO sample as a whole with representative samples at high redshift could probe redshift evolution of galaxy properties. Even though many high-redshift samples only probe galaxies with Hα luminosities of more than 10^{42} erg s^{-1}, this does not mean that the $z \simeq 2$ samples are necessarily 'tip of the iceberg' samples covering only a highly biased fraction of the population. Instead, the median SFR for a fixed stellar mass evolves upward (by a factor of 3 from $z = 0.36$ to $z = 0.98$, Noeske et al. 2007) and continues to increase to $z \sim 2$ (Daddi et al. 2007). Both our sample and samples at high redshift can probe properties of the star formation 'main sequence' – the relationship between SFR in galaxies and their stellar mass (Noeske et al. 2007). Finally, we could compare galaxies between eras based on their distance above the star formation main sequence, which could probe the origins of such 'star bursts.' Each of these comparisons potentially test very different kinds of 'evolution' between $z \simeq 2$ and today. We will explore these different comparisons below and in future papers of this series.

2.2 Sample selection biases

Our sample selection criteria impose a lower limit on the galaxy continuum luminosity and stellar mass for included galaxies. To be included in the SDSS spectroscopic sample from which we have selected our sample, the galaxy must have $r \lesssim 17.77$ mag (Strauss et al. 2002). This corresponds to an absolute magnitude of $M_r < -19.4$ and -21.5 mag in the two redshift windows around 0.07 and 0.13, respectively. These limits on continuum luminosity translate to implicit mass limits of roughly 10^9 M$_\odot$ for the $0.055 < z < 0.084$ redshift range, and roughly 10^{10} M$_\odot$ for the $0.124 < z < 0.151$ redshift range (see Fig. 2). Particularly for the low-redshift range, the sample probes a broad range in stellar mass of $\sim 10^9$ to 10^{11} M$_\odot$.

Galaxies hosting active nuclei have been excluded because such active nuclei can significantly bias estimates of SFR based on the Hα emission line. The star-forming sample of Brinchmann et al. (2004) already has active galactic nuclei removed. To define galaxies as star forming, Brinchmann et al. use the criteria of Kauffmann et al. (2003b), which are based on the Baldwin, Phillips & Terlevich (1981, BPT) diagram. To be included in the sample, galaxies must have been detected at a level of 3σ in each of four diagnostic lines (Hα λ6563, [N II] λ6584, [O III] λ5007 and Hβ λ4861). The detection requirement in these four lines may introduce some selection bias, as described in detail in Brinchmann et al. (2004). The strongest bias is from the strength of the [O III] λ5007 line, which varies inversely

Downloaded from http://mnras.oxfordjournals.org/ at Liverpool John Moores University on October 27, 2016

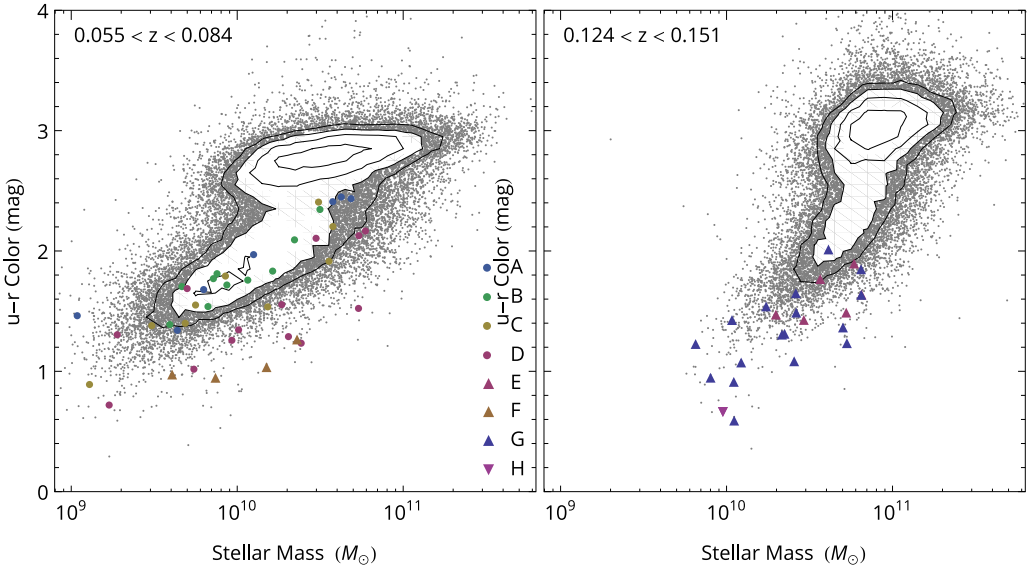

Figure 2. The $u - r$ colours and masses for the SDSS spectroscopic sample are shown by the grey points and contours for the two redshift ranges of our selection criteria. Galaxies making up the DYNAMO selection within each redshift range are highlighted with coloured symbols. The symbol shape and colour correspond to the selection window as shown in the key, and match the symbol coding of Fig. 1. The impact of the limit of SDSS spectroscopy to apparent r-band magnitude less than 17.7 is reflected in the range of stellar masses included in each redshift range: $\gtrsim 10^9$ for the lower redshift range and $\gtrsim 10^{10}$ for the higher redshift range.

with galaxy stellar mass. Our star-forming requirement eliminates approximately half of all galaxies with detectable Hα emission from star formation in SDSS.

No correction for dust extinction has been included in the selection. This may bias the sample away from extremely dusty galaxies, even if they have high rates of star formation. Also, our selection on Hα luminosity is effectively a selection on Hα central surface brightness because of the small aperture for the SDSS fibre spectroscopy. If they are sufficiently common, galaxies with significant star formation only in regions beyond the fibre coverage could still be included in our sample through our inclusion of galaxies with lower (central) luminosities. However, if such galaxies are rare, then they could be missed by our selection strategy.

3 OBSERVATIONS

Integral-field spectroscopic data were obtained using two different telescopes; the 3.9 m Anglo–Australian Telescope and the ANU 2.3 m Telescope, both situated at Siding Spring Observatory, Australia. Table 2 lists our observing runs and instrument configurations. Table 3 lists the telescope used, observation date and exposure time for each galaxy in our sample. The observing procedures and data-reduction techniques are described separately for each telescope.

3.1 SPIRAL

The SPIRAL integral-field unit was used with the AAOmega spectrograph (Sharp et al. 2006) on the Anglo–Australian Telescope. SPIRAL is an array of 32 × 16 square, 0.7 arcsec lenslets situated at the Cassegrain focus. This provides a contiguous integral field of 22.4 arcsec × 11.2 arcsec on the sky. The long axis of the field was set to be east–west for all observations. Light from the lenslets is fed by fibre-optic cable into AAOmega, a two-arm spectrograph. The incoming light is split by a dichroic mirror into the two spectrograph arms. Each arm is fitted with interchangeable, volume-phase holographic gratings. Both the grating angle and the camera angle are set to achieve optimum throughput for the desired wavelength range.

Table 2. Observing runs.

Program	Date	Moon[a]	Weather
SPIRAL-08A	2008 Jul 13	0.799	Not photometric
SPIRAL-08A	2008 Jul 14	0.870	Clear
SPIRAL-08A	2008 Jul 15	0.927	Occasional cloud
SPIRAL-08A	2008 Jul 16	0.970	Clear
SPIRAL-09A	2009 Jun 5	0.952	Occasional cloud
SPIRAL-DD[b]	2010 Jan 16	0.014	Not photometric
SPIRAL-DD	2010 Jan 17	0.044	Windy, clear
SPIRAL-DD	2010 Jan 18	0.090	Clear, photometric
SPIRAL-DD	2010 Jan 19	0.150	Not photometric
WiFeS-09D	2010 Jan 19	0.150	Photometric
WiFeS-09D	2010 Jan 20	0.224	Photometric
WiFeS-09D	2010 Jan 21	0.309	Photometric
WiFeS-09D	2010 Jan 22	0.403	Photometric

[a]Fraction of moon illuminated at mid-night.
[b]DD – Director's discretionary time.

We used the 570 nm dichroic and the 1700I grating in the red spectrograph. These provided a nominal spectral resolving power of $R \simeq 12\,000$ and a wavelength coverage of 500 Å. The blaze angle of the volume-phase holographic grating was set so that the wavelength coverage included the Hα line for the redshift range of galaxies observed during a particular night. Data from the blue spectrograph were not used.

Data were obtained over three observing runs on 2008 July 13–16, 2009 June 5 and 2010 January 16–19. Exposures of a quartz-halogen lamp were obtained during each afternoon for spectral and spatial flat-fielding. Exposures of copper–argon and iron–argon arc lamps were obtained for wavelength calibration. The typical instrumental full width at half-maximum (FWHM) was 2.5 pixels (measured from arc lines) or about 30 km s^{-1}. The wavelength calibration was confirmed to be stable through the night using repeated arc-lamp

Downloaded from http://mnras.oxfordjournals.org/ at Liverpool John Moores University on October 27, 2016

Table 3. SDSS target information.

Name	Sel.	ID	SDSS SpecObjID[a]	Obs date	Instrument	$T_{\rm exp}^{b}$ (s)	Seeing[c] (arcsec)
SDSS J040242.50−06:44:47.7	A	04-3	130827332481974272	2010 Jan 16	AAT/SPIRAL	3600	2.1
SDSS J04023.187−05:16:29.2	A	04-4	130827334742704128	2010 Jan 17	AAT/SPIRAL	7200	1.4
SDSS J083751.79+06:16:9.58	A	08-3	334337177892683776	2010 Jan 16	AAT/SPIRAL	7200	1.3
SDSS J08488.126+04:15:33.5	A	08-4	335181439442092032	2010 Jan 17	AAT/SPIRAL	7200	4.0
SDSS J104746.94−00:22:4.24	A	10-1	77628570993688576	2010 Jan 16	AAT/SPIRAL	5400	1.0
SDSS J104638.40+01:48:31.6	A	10-2	142932668890218496	2010 Jan 17	AAT/SPIRAL	7200	4.0
SDSS J135232.50+02:43:30.6	A	13-2	149405190099828736	2009 Jun 5	AAT/SPIRAL	7200	1.1
SDSS J040828.64−04:52:19.8	B	04-3	131108818087051264	2010 Jan 19	2.3 m/WiFeS	7200	1.2
SDSS J040228.88−05:20:24.5	B	04-4	131108817319493632	2010 Jan 20	2.3 m/WiFeS	7200	1.2
SDSS J084735.35+09:31:2.56	B	08-3	495623963607564288	2010 Jan 19	2.3 m/WiFeS	7200	1.2
SDSS J08543.867+07:34:52.2	B	08-4	365863508732018688	2010 Jan 20	2.3 m/WiFeS	7200	1.2
SDSS J105918.14+09:48:37.1	B	10-1	343625916930326528	2009 Jun 5	AAT/SPIRAL	3600	1.5
SDSS J111635.58+02:33:48.1	B	11-2	143777215144787968	2010 Jan 20	2.3 m/WiFeS	7200	1.2
SDSS J144452.04+04:36:54.5	B	14-1	165449263151579136	2009 Jun 4	AAT/SPIRAL	1200	1.5
				2009 Jun 5	AAT/SPIRAL	2400	1.5
SDSS J154413.93+03:45:50.6	B	15-1	167419669911699456	2009 Jun 5	AAT/SPIRAL	3600	1.0
SDSS J151129.57−02:05:21.1	B	15-2	260026477938999296	2009 Jun 5	AAT/SPIRAL	3600	1.0
SDSS J205912.10−06:07:40.6	B	20-1	179242181897224192	2009 Jun 5	AAT/SPIRAL	7200	1.1
SDSS J00288.639−00:39:10.2	C	00-1	110279118452424704	2008 Jul 15	AAT/SPIRAL	3600	1.4
SDSS J04109.301−06:05:10.5	C	04-1	131108816509992960	2010 Jan 21	2.3 m/WiFeS	3600	1.2
SDSS J040425.99−05:22:13.2	C	04-2	131108817516625920	2010 Jan 21	2.3 m/WiFeS	3600	1.2
SDSS J132639.42+01:30:1.47	C	13-1	148562120957493248	2008 Jul 15	AAT/SPIRAL	3600	1.3
SDSS J13430.490+03:53:19.3	C	13-3	240604571322286080	2008 Jul 15	AAT/SPIRAL	3600	1.5
SDSS J143342.60−00:48:0.23	C	14-2	86353122502377472	2008 Jul 15	AAT/SPIRAL	3100	–
SDSS J205259.06−06:04:28.7	C	20-2	179242181045780480	2008 Jul 15	AAT/SPIRAL	3600	1.9
SDSS J213919.76−08:41:42.6	C	21-1	331522925825884160	2008 Jul 15	AAT/SPIRAL	3600	–
SDSS J223949.34−08:04:18.0	C	22-2	203449235771752448	2008 Jul 15	AAT/SPIRAL	3600	1.3
SDSS J004324.43+00:00:59.0	D	00-2	110842120222277632	2008 Jul 14	AAT/SPIRAL	2400	1.3
SDSS J103235.52+07:06:6.84	D	10-4	281419573666775040	2010 Jan 22	2.3 m/WiFeS	3600	1.4
SDSS J133047.05+01:42:31.5	D	13-1	148562120336736256	2008 Jul 14	AAT/SPIRAL	3600	1.4
SDSS J13307.005+00:31:53.3	D	13-5	83821232935403520	2008 Jul 13	AAT/SPIRAL	3600	1.4
SDSS J14468.569+00:51:51.4	D	14-1	151375517637935104	2008 Jul 14	AAT/SPIRAL	3600	1.4
SDSS J15437.078−01:08:3.98	D	15-1	260870942786322432	2008 Jul 13	AAT/SPIRAL	3600	–
SDSS J15435.269−01:46:42.4	D	15-2	260870941217652736	2008 Jul 13	AAT/SPIRAL	2400	1.6
SDSS J153435.39−00:28:44.5	D	15-3	88886509838532608	2008 Jul 14	AAT/SPIRAL	3600	1.2
SDSS J20529.089−00:30:39.3	D	20-1	276915143844036608	2008 Jul 14	AAT/SPIRAL	3600	1.1
SDSS J211733.50−00:08:5.02	D	21-3	278041387637669888	2008 Jul 14	AAT/SPIRAL	3600	1.3
SDSS J221614.50+12:23:43.8	D	22-1	207389871029878784	2008 Jul 14	AAT/SPIRAL	3600	1.3
SDSS J223745.27−08:39:22.5	D	22-2	203449235545260032	2008 Jul 14	AAT/SPIRAL	3600	1.3
SDSS J234957.74+00:05:22.9	D	23-1	108871770764738560	2008 Jul 14	AAT/SPIRAL	3600	–
SDSS J00561.343+00:43:30.0	E	00-2	111124108015566848	2008 Jul 16	AAT/SPIRAL	1800	–
SDSS J005453.56−00:59:8.52	E	00-3	111124105498984448	2008 Jul 16	AAT/SPIRAL	3600	1.0
SDSS J040530.53−05:43:22.0	E	04-1	131108816992337920	2010 Jan 19	AAT/SPIRAL	3600	0.9
SDSS J093412.85+10:40:35.4	E	09-1	490275791427338240	2010 Jan 19	AAT/SPIRAL	3600	1.3
SDSS J101940.29−00:26:24.7	E	10-1	76502554946568192	2010 Jan 19	AAT/SPIRAL	3600	1.6
SDSS J235833.89+14:54:45.3	E	23-1	211330581978415104	2008 Jul 16	AAT/SPIRAL	1800	1.5
SDSS J08311.931+04:03:18.9	F	08-2	333773945712934912	2010 Jan 21	2.3 m/WiFeS	3600	1.2
SDSS J091929.43+06:10:55.3	F	09-1	279168078305034240	2010 Jan 21	2.3 m/WiFeS	3600	1.2
SDSS J102715.47+06:50:3.66	F	10-1	281419573087961088	2010 Jan 21	2.3 m/WiFeS	3600	1.2
SDSS J122534.26−02:50:29.0	F	12-4	94235951454224384	2010 Jan 21	2.3 m/WiFeS	3600	1.2
SDSS J034857.51−00:42:54.2	G	03-2	349819129932283904	2010 Jan 18	AAT/SPIRAL	3600	1.7
SDSS J032718.58−00:28:30.5	G	03-4	116753553971740672	2010 Jan 19	AAT/SPIRAL	3600	1.0
SDSS J041219.71−05:54:48.6	G	04-1	131108815939567616	2010Jan 18	AAT/SPIRAL	3600	1.8
SDSS J08456.474+02:46:15.4	G	08-1	158976187991851008	2010 Jan 18	AAT/SPIRAL	3600	2.0
SDSS J085347.72+06:51:6.87	G	08-2	334899956504592384	2010 Jan 18	AAT/SPIRAL	3600	2.0
SDSS J080412.52+07:09:58.5	G	08-3	494498037406629888	2010 Jan 18	AAT/SPIRAL	3600	1.9
SDSS J08276.707+04:19:23.0	G	08-4	333773945297698816	2010 Jan 19	AAT/SPIRAL	3600	1.1
SDSS J085418.73+06:46:20.6	G	08-5	334899956882079744	2010 Jan 19	AAT/SPIRAL	3600	1.3
SDSS J091210.96+10:04:12.0	G	09-1	489712833139834880	2010 Jan 19	AAT/SPIRAL	3600	1.3
SDSS J102142.47+12:45:18.7	G	10-1	491683209700966400	2010 Jan 18	AAT/SPIRAL	3600	2.1
SDSS J113520.16+11:12:42.1	G	11-1	452558278207995904	2010 Jan 18	AAT/SPIRAL	1800	1.8
SDSS J135022.74−02:51:57.5	G	13-1	257211852017106944	2008 Jul 16	AAT/SPIRAL	3600	1.5
SDSS J145428.33+00:44:34.3	G	14-1	87199082266755072	2008 Jul 16	AAT/SPIRAL	3600	1.1

Downloaded from http://mnras.oxfordjournals.org/ at Liverpool John Moores University on October 27, 2016

Table 3 – *continued*

Name	Sel. ID		SDSS SpecObjID[a]	Obs date	Instrument	T^b_{exp} (s)	Seeing[c] (arcsec)
SDSS J145435.35−02:00:49.7	G	14-3	259463424658898944	2008 Jul 16	AAT/SPIRAL	3600	1.8
SDSS J203724.58−06:22:0.33	G	20-1	178679178873274368	2008 Jul 16	AAT/SPIRAL	3600	1.1
SDSS J20442.915−06:46:57.9	G	20-2	178960572606316544	2008 Jul 16	AAT/SPIRAL	3600	0.9
SDSS J211911.80+01:08:31.9	G	21-2	278041388019351552	2008 Jul 16	AAT/SPIRAL	1800	1.1
SDSS J104431.76+12:09:25.2	H	10-2	450869566705238016	2010 Jan 22	2.3 m/WiFeS	3600	1.4

[a]The SDSS spectroscopic id number from data release four (Adelman-McCarthy et al. 2006).
[b]The total exposure time for the night. See Section 3 for the lengths of individual exposures.
[c]The full width at half-maximum seeing observed on a nearby star as part of the observation sequence.

observations and measurements of sky lines in each exposure. Since the bias level on the red AAOmega camera is stable and we observed no structure in the bias frames, we chose not to record separate bias frames, but subtracted an overscan bias in our data reduction.

We took three 1200 s exposures for targets with SDSS fibre Hα fluxes of greater than 3.0×10^{-15} erg s^{-1} cm^{-2} (selection windows C–I, Fig. 1). The telescope was offset by a single spatial pixel between each dithered exposure to mitigate the effects of a few dead fibres and detector defects. For fainter targets (selection windows A and B, Fig. 1), we repeated this procedure twice for a total on-source integration time of 7200 s. In two cases (selection IDs G 21-2 and E 0-2), the galaxy was much larger than the SPIRAL field of view, and spatial mosaicking was necessary. Mean seeing was 1.4 arcsec FWHM, which corresponds to a physical resolution of 1.5–3.6 kpc depending on redshift.

Wavelength- and spatially calibrated data cubes were first extracted from the raw data using the standard 2DFDR data reduction facility for this instrument (Sharp et al. 2006). Briefly, this uses an optimal-extraction routine to remove crosstalk between fibres in the raw CCD image, and then rectifies the data using the arc-lamp images. The basic reduction was then completed using custom-written IDL[3] scripts.

A sigma-clipped mean was used to simultaneously combine frames and remove cosmic rays and other glitches. First, the frames were median combined. This median provided the information to construct a noise estimate for each pixel in the image (including read noise). For each frame, outliers greater than 8σ were masked. The frames were then combined by averaging the unmasked pixels across individual frames.

A two-step, iterative process was used to subtract sky emission. First, an approximate sky spectrum was generated by median combining spectra from all spatial locations in the image. This approximate sky spectrum was then subtracted from the whole cube, and the residual flux in each spaxel summed. This residual flux image represents object photons. We identified a residual surface-brightness limit in this image by eye and deemed spaxels with residual surface brightnesses below this limit to contain only sky emission. The spectra for these spaxels (typically 20–40 per cent of the field of view) were then median combined to produce a final sky spectrum. This final sky spectrum was then subtracted from the whole cube.

The flux calibration for SPIRAL was achieved in two stages. First, a spectro-photometric standard star was observed each night. With this observation, we calibrated the relative throughput of the telescope-instrument system as a function of wavelength. Secondly, the flux in the central 3 arcsec of the galaxy was scaled to match the flux measured by the SDSS pipeline. This scaling corrects for the variation in fibre throughput due to flexing of the fibre bundle, and corrects for varying transparency on many of the nights SPIRAL was used.

3.2 WiFeS

We used the wide-field spectrograph (WiFeS; Dopita et al. 2007) on the ANU 2.3 m Telescope. WiFeS is an image-slicing integral-field spectrograph. WiFeS provides a 25 by 38 arcsec field of view sampled with either 1.0×0.5 or 1.0×1.0 arcsec spatial pixels (the latter being achieved with 1×2 CCD binning). The spectrograph has two arms with interchangeable dichroics and fixed gratings. We chose the 615 nm dichroic and the I7 000 grating for the red side, which provided a spectral resolving power of $R \simeq 7000$ and 6832–9120 Å wavelength coverage. The data were taken on 2010 January 16–24. The mean seeing was 1.2 arcsec, corresponding to a physical resolution of 1.3–3.2 kpc for the redshift range of our galaxies. Data from the blue spectrograph are not considered here.

Calibration frames were taken each afternoon, including bias frames, quartz-iodide flat-field frames and arc-lamp frames. The wavelength solutions were checked against identical arc-lamp frames taken at the end of the night, and were stable through the night. Except for bias subtraction, the reductions took advantage of the WiFeS data-reduction pipeline (Dopita et al. 2010), which includes flat-fielding and both spatial and spectral rectification.

For targets with SDSS fibre Hα fluxes of greater than 3.0×10^{-15} erg s^{-1} cm^{-2} (selection windows C–I, Fig. 1), we obtained two 1800 s exposures with no on-detector binning. For fainter targets, we recorded 4×1800 s exposures, with 1×2 on-detector pixel binning along the spatial axis. We dithered the telescope 2 arcsec in different directions between exposures to ensure detector artefacts could be averaged out. As the WiFeS field of view is larger than all of our targets, we did not employ any mosaicking.

Flat-fielding, sky subtraction and rectification were all accomplished using the standard WiFeS reduction pipeline (Dopita et al. 2010), written in IRAF[4] (Tody 1993). For the sky subtraction, a sky region was identified in each observation to estimate the sky spectrum. Spectra in this region were combined to create a master sky spectrum that was then subtracted from each spectrum in the rectified data cube.

The individual frames were median combined using *imcombine* in IRAF to form final data cubes, and to remove cosmic rays.

The data were flux calibrated using observations of a spectro-photometric standard star taken on each night. The WiFeS

[3] IDL: Interactive Data Language

[4] IRAF is distributed by the National Optical Astronomy Observatories, which are operated by the Association of Universities for Research in Astronomy, Inc., under cooperative agreement with the National Science Foundation.

Downloaded from http://mnras.oxfordjournals.org/ at Liverpool John Moores University on October 27, 2016

observations were obtained on photometric nights and WiFeS does not suffer from the fibre-related throughput variations of SPIRAL, so accurate absolute flux calibrations were obtained. Repeat observations of standards at the beginning and end of the night were used to confirm the stability of the flux calibration. Fluxes measured from the central 3 arcsec of each observed galaxy agree within a few per cent with those measured by SDSS.

4 DATA ANALYSIS

4.1 Emission-line fitting

The wavelength range of our data generally includes five bright emission lines that are all well resolved spectrally; [N II] λ6548, Hα λ6563, [N II] λ6584, [S II] λ6717 and [S II] λ6731. Continuum emission is detected from a few objects. The continuum is estimated using a 300 pixel moving median filter, and subtracted. This is the same technique used by the SDSS pipeline (Adelman-McCarthy et al. 2006). The resulting spectrum contains only emission lines.

Our custom IDL code fits a synthetic spectrum consisting of five Gaussian spectra (one for each line) to the observed spectrum. Line widths in the synthetic spectrum are initially set to the instrumental resolution, as determined by arc lines, and then the best-fitting broadening is determined during the fitting process. Thus, the dispersion values we quote are intrinsically corrected for instrument broadening. This approach is superior to the alternative of subtracting the instrumental line width in quadrature, which is problematic at low signal-to-noise ratios (Förster Schreiber et al. 2009). The redshifts of the five lines are assumed to be the same, but the flux and width of the lines are allowed to vary independently. A Levenberg–Markwardt minimization algorithm is used to fit the data (Markwardt 2009).

Once the fitting is completed, a mask is created to exclude regions having low signal-to-noise ratio from further analysis. First, we compute the median absolute deviation of each reduced spectrum to give an estimate of the typical noise at each spatial position in the data cube. The median absolute deviation estimates the width of the distribution of intensities in the continuum-subtracted spectrum. It is robust against outliers, including emission lines in the spectrum, bad pixels and edge effects. We then compute the significance of an Hα detection as the ratio of its total fit flux (integrated across the line) to this width of the intensity distribution. Spectra with signal-to-noise ratios less than three are masked automatically. This mask was reviewed by eye interactively, and invalid fits were removed (typically a few per galaxy). All measurements reported below were performed within the unmasked region.

The results of our emission-line fitting are shown in the online data for this paper as maps of continuum-subtracted Hα emission, velocity and velocity dispersion for each galaxy in our sample.

Fig. 3 illustrates the quality of the data for one of our galaxies, D 15-3. The spectrum in the region of the Hα emission line at each spatial location in the data is shown in the corresponding box of the figure. Underplotted in green is the best fit to the Hα emission line. Most of the spectra are well fitted by a single Gaussian profile. Spectra in the top-left quadrant of Fig. 3 are blueshifted relative to the systemic velocity (shown by the vertical dashed line in each box), and those in the lower-right quadrant are predominantly redshifted. Some spectra show more complex emission-line structure than a simple Gaussian. Many of these are located near the rotation axis, and consist of blended blueshifted and redshifted emission. These spectra are fit by a single Gaussian of larger width as a result of this beam smearing. Other subtle line asymmetries are apparent in Fig. 3, which we have ignored in this analysis.

4.2 Aperture effects

The effect on our sample selection of the 3 arcsec-diameter SDSS optical fibres has been noted in Section 2.1. We now quantify the amount by which the actual Hα luminosities of our galaxies exceed those predicted from SDSS spectra. We use our integral-field data cubes to compare the Hα flux within a 3 arcsec-diameter aperture to the total emission-line flux (excluding masked regions; Section 4.1). These fluxes are shown in Fig. 4. On average, the Hα flux of the whole galaxy is 0.63 dex larger than the region covered by the SDSS fibre, with a root-mean-square scatter of 0.26 dex. This offset is indicated by the dashed line in Fig. 4. We use the total Hα flux in our subsequent analysis.

4.3 Classification of galaxies by kinematic morphology

Integral-field spectroscopy of galaxies at high redshift reveals their kinematic morphologies to be markedly different from those of galaxies at low redshift. Rotating galaxies at high redshift often have turbulent, geometrically thick discs (Elmegreen & Elmegreen 2006; Förster Schreiber et al. 2006, 2009; Genzel et al. 2006). Additionally, there are both many merging galaxies and many 'dispersion-dominated' galaxies (having velocity shears smaller than their velocity dispersions). Conversely, most of the galaxies sampled by the GHASP survey look more like quiescent, thin discs (Epinat et al. 2010). Results from the IMAGES survey suggest that the fraction of rotating, disc-like galaxies changes with time (Yang et al. 2008). We define a classification scheme and classify our galaxies for comparison with other galaxy samples.

Our sample of galaxies is classified into three different general kinematic morphologies using a variation of the system described by Flores et al. (2006) for the IMAGES survey. Although other approaches have been suggested for classifying the kinematic morphologies of high-redshift galaxies (e.g. Shapiro et al. 2008; Förster Schreiber et al. 2009), the IMAGES system is based on simple visual criteria that can be applied to data with high noise or low resolution. The IMAGES classification defines three distinct categories: rotating discs (RD), perturbed rotators (PR) and complex kinematics (CK). We supplement the classification with the subcategories for compact galaxies that otherwise fit into the original three categories. Our classification system is defined as follows.

(i) Rotating discs (RD, ●) – RD galaxies show typical kinematic features of a disc; the velocity field is qualitatively consistent with rotation, the velocity dispersion peak corresponds to the centre of rotation,[5] and the axis of rotation aligns with the minor axis seen in SDSS *gri* imaging. These are the same features displayed by the best-case rotation-dominated galaxies of Förster Schreiber et al. (2009).

(ii) Perturbed rotators (PR, ■) – Galaxies with perturbed rotation meet all the criteria for the RD classification except those for the velocity-dispersion map. For PR classification, either the peak of the velocity dispersion is offset from the centre of rotation by more than 3 kpc, or there is no distinct peak.

[5] This peak in velocity dispersion corresponds to where the local velocity gradient is steepest, and is caused by beam smearing as described in Section 4.5.

Downloaded from http://mnras.oxfordjournals.org/ at Liverpool John Moores University on October 27, 2016

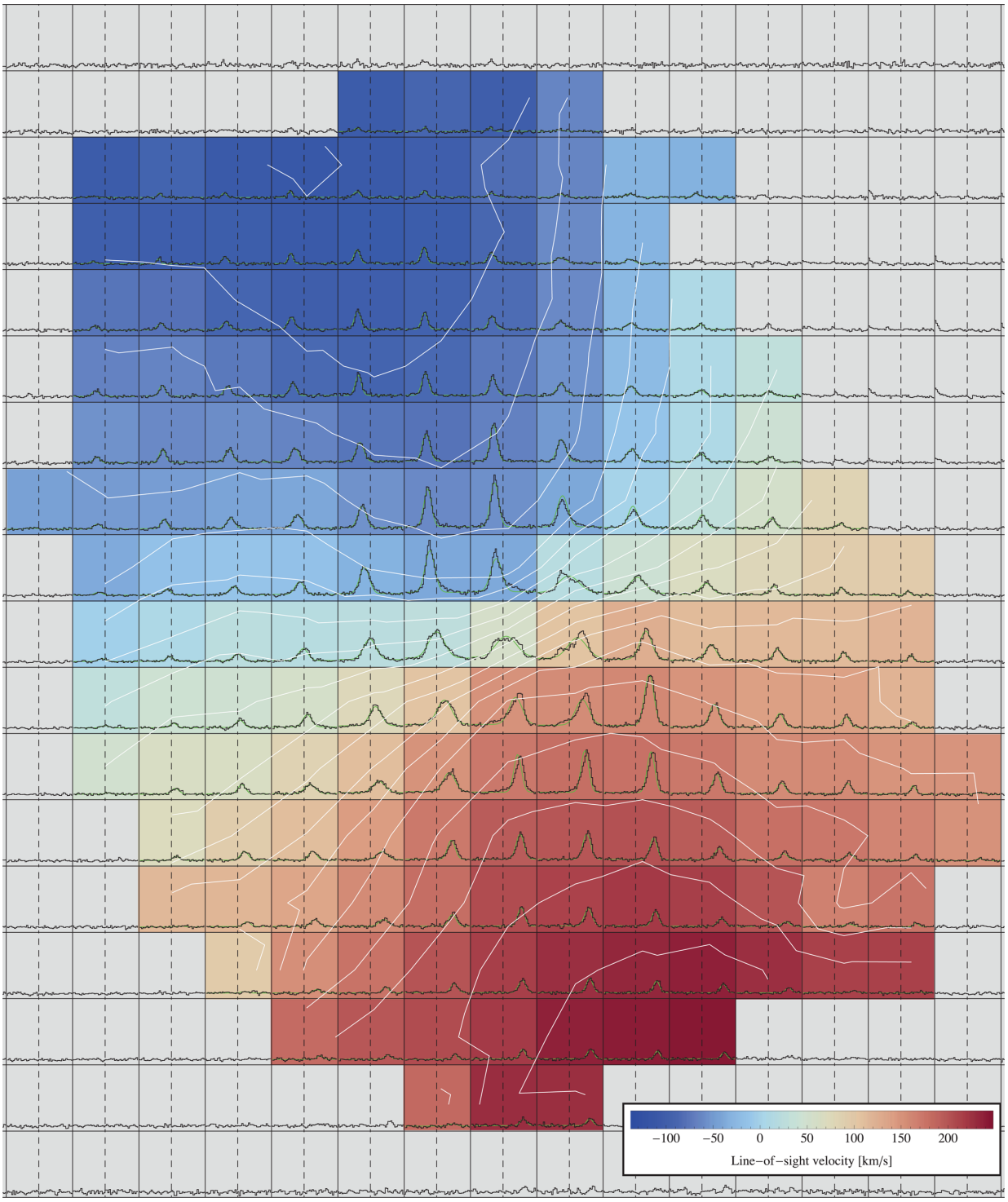

Figure 3. The spatial map of spectra in the region around the Hα emission line for D 15-3. This galaxy has an integrated SFR of 13.7 $M_\odot$ yr^{-1}, a stellar mass of 5.4×10^{10} $M_\odot$ and a velocity dispersion of $\sigma_m = 30.6$ km s^{-1}. Each grid square shows the object spectrum (black) in the 14 Å region around the Hα emission line for the corresponding spatial location from our integral-field spectroscopic data. North is up, east is to the left. The flux scale (in arbitrary units) is the same in all squares. Underplotted in green is the Gaussian fit (Section 4.1). The dashed vertical line in each square shows the systemic redshift of Hα for this galaxy. The background colour of each square corresponds to the line-of-sight velocity of the Hα emission in that spatial pixel relative to the systemic redshift as shown by the key in the lower left (i.e. the velocity map). Masked pixels where the fit to the Hα emission failed have a grey background. Overlaid in white are lines of constant velocity, separated by 20 km s^{-1}. These reveal the 'spider-diagram' shape to the velocity field, which helps identify this galaxy as a RD. This galaxy shows the skewing and splitting of the emission-line profile due to beam smearing near the centre.

Downloaded from http://mnras.oxfordjournals.org/ at Liverpool John Moores University on October 27, 2016

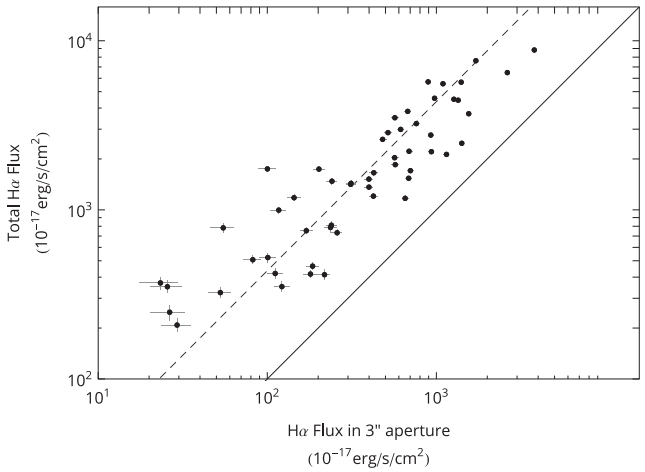

Figure 4. Ratio of fibre aperture flux to total flux (excluding masked regions) for the Hα emission line. The solid line shows the 1–1 relation, while the dashed line is offset by the median 0.63 dex observed across our sample.

(iii) Complex kinematics (CK, ▲) – Galaxies that do not meet the criteria for either the RD or PR categories are classified as CK. This category includes galaxies for which both velocity and velocity dispersion vary significantly from regular discs, or where the rotation axis is significantly misaligned with the optical axis. Objects with multiple approaching and receding regions ('multipolar' velocity fields) are also assigned in this classification.

(iv) Compact (cRD, ○; cPR, □; cCK, △)– a large fraction of our sample is compact (25 of 67), and these are given separate classifications. Compact galaxies have *r*-band exponential scalelengths of less than 3 kpc as measured by SDSS[6] (2.3 arcsec at $z \simeq 0.07$, 1.2 arcsec at $z \simeq 0.14$). They are otherwise classified exactly as above. The classification is less reliable for these compact galaxies because they are not as well resolved, which is why we found this a useful distinction.

The results of our classification are included in Table 5. Of the sample of 67, 25 galaxies are classified as RD, and six are classified as PR. We are confident these 31 RD and PR galaxies are indeed rotating, disc-like galaxies, as the classification is corroborated by results from the TFR, which we discuss below in Section 5.4. A further 20 galaxies are cRD, and five are classified cPR. These galaxies, while meeting the classification criteria for their RD and PR counterparts, have small angular sizes, and so the classification may be affected by limited resolution. Of the remaining galaxies, five are classified CK and six as cCK. These galaxies with CK are most likely mergers, although the classification only clearly defines them as not disc-like. Of the whole sample, 46 per cent show all the signatures of RD galaxies, while 16 per cent show no indication of global rotation. Most of the remaining 37 per cent show some evidence of RD. For the 27 galaxies in our sample with SFR greater than 10 $M_\odot$ yr^{-1}, seven are classified RD and one is PR, making 30 per cent rotating. A further nine are classified cCK or CK. The remaining 10 galaxies show marginally resolved indications global rotation (cRD and cPR).

[6] SDSS's `expRad_r` in the `PhotoObj` view.

4.4 Disc fitting

Model discs have been fit to the velocity maps for all of our sample galaxies. A simple disc model has been adopted, in line with disc models used to fit integral-field spectra of galaxies at high redshifts (e.g., Förster Schreiber et al. 2009, see Epinat et al. 2010 for a review of different models).

The model velocity field is created as follows. First, we create a spatial map of intrinsic velocities projected along the line of sight. The rotation curve is parametrized by

$$\boldsymbol{V}(\boldsymbol{r}) = \frac{2V_{\rm asym}}{\pi} \arctan\left(\frac{|\boldsymbol{r}|}{r_t}\right)(\hat{r} \times \hat{z}), \quad (1)$$

where $V_{\rm asym}$ is the asymptotic circular velocity, and r_t is the kinematic scale radius (Courteau 1997). The spatial vector $\boldsymbol{r}$ points to the location within the plane of the disc. The unit vector $\hat{r}$ is parallel to $\boldsymbol{r}$, and the unit vector $\hat{z}$ points perpendicular to the plane of the disc. The velocity $\boldsymbol{V}$ is projected along the line of sight to produce the velocity map. Secondly, we use the velocity map to define an intensity cube with the same spatial coordinates and a velocity coordinate. The spatial intensities are for an exponential surface-brightness profile (using scalelengths from SDSS *r*-band photometry). The intensities along the velocity dimension are a Gaussian profile that is centred on the line-of-sight velocity from the map. The width of the profile corresponds to a constant intrinsic velocity dispersion across the model, $\sigma_{\rm model}$. Also included as free parameters are the kinematic centre of the disc, and a systemic velocity offset (which allows for errors in redshift). Next, the intensity cube is convolved with a three-dimensional Gaussian kernel. The spatial FWHM of the kernel is set to the seeing FWHM measured during observation of the corresponding galaxy, and the velocity FWHM is set to the instrumental resolution measured from arc-lamp lines. This convolution or 'beam smearing' raises the central velocity dispersion of the model. Finally, the intensity cube, which is analogous to an observed data cube, is collapsed into maps of velocity and velocity dispersion by computing moments of the intensity distribution. The final velocity and velocity-dispersion maps can then be compared with the observed data.

We define the quality of the fit as χ^2. This standard quality is defined as

$$\chi^2 = \sum_{\rm pix} \frac{\left(v_{\rm pix,model} - v_{\rm pix,obs}\right)^2}{E(v_{\rm pix,obs})^2} + W \sum_{\rm pix} \frac{\left(\sigma_{\rm pix,model} - \sigma_{\rm pix,obs}\right)^2}{E(\sigma_{\rm pix,obs})^2}. \quad (2)$$

Here, v and σ are the velocity and velocity dispersions, respectively. $E(x)$ gives the error on the corresponding observation. The weighting, W, sets the relative importance of the two different physical phenomenon to quality of the fit. We weight the velocity map higher to ensure a good fit to the observed velocity field ($W = 0.2$). χ^2 is minimized by varying the free parameters using a Levenberg–Markwardt routine. Our model has six free parameters ($V_{\rm asym}$, $\sigma_{\rm model}$, r_t, position angle, horizontal and vertical spatial centring, and velocity offset). Inclination and circular velocity are nearly degenerate parameters (Begeman 1989; Epinat et al. 2010), so we fix inclination, the seventh parameter, to that measured by the SDSS photometric pipeline for the *r*-band exponential disc fit.[7] Because we have weighted the velocity map highly in the fit, we find that the model velocity dispersion parameter often is not representative, and we do not present it here. The velocity map of the

[7] This is parameter `expAB_r` in the `PhotoObj` view.

Downloaded from http://mnras.oxfordjournals.org/ at Liverpool John Moores University on October 27, 2016

best-fitting model and its difference from the observed velocity map for each galaxy are included in the online data for this paper. For galaxies visually classified as CK or cCK (Section 4.3), these fits are questionable, so they are not used in our analysis.

The rotation curve that fits best is used to compute a characteristic circular velocity for Tully–Fisher analysis in Section 5.4. The $V_{\rm asym}$ of our fit is not suitable as a characteristic velocity because it is often much higher than the maximum velocity observed due to the shape of the arctangent-like rotation curve of our model. The model velocity at a radius of 2.2 r-band exponential disc scalelengths,[8] $V_{2.2R_r}$, is more suitable (Miller et al. 2011). This is where the rotation curve of an ideal, self-gravitating, exponential disc would peak (Freeman 1970), and is more comparable to other Tully–Fisher type analyses. Therefore, we adopt this value as the characteristic circular velocity for all galaxies in our sample except those classified as CK and cCK. The values are listed in Table 5.

4.5 Non-parametric velocity dispersion

We characterize the velocity dispersion of the gas in our galaxies using the $\sigma_{\rm m}$ measure of Law et al. (2009) on the Hα emission, but corrected for the effects of unresolved disc rotation. The quantity $\sigma_{\rm m}$ is defined to be the intensity (I) weighted mean of the velocity dispersion measured in individual spatial pixels ($\sigma_{\rm pix}$):

$$\sigma_{\rm m} = \frac{\sum \sigma_{\rm pix} I_{\rm pix}}{\sum I_{\rm pix}}. \quad (3)$$

Within each pixel, the intensity, $I_{\rm pix}$, is the flux, and the velocity dispersion, $\sigma_{\rm pix}$, is the width, of the best-fitting Gaussian profile of Hα emission (Section 4.1). Effectively, $\sigma_{\rm m}$ measures the velocity dispersion after removing velocity shear larger than the spatial resolution element. The statistical error on $\sigma_{\rm m}$ for our sample is typically 1–2 km s^{-1}, and we have verified this estimate with the difference of $\sigma_{\rm m}$ computed on alternating checker-board masks of the full data for each galaxy. Note that the variation of $\sigma_{\rm pix}$ across each galaxy is typically much larger than the error, and reflects real variation in the turbulence across the galaxy.

The flux-weighted mean velocity dispersion, $\sigma_{\rm m}$, has been widely adopted for characterizing the velocity dispersion of star-forming gas in galaxies at high redshift (Law et al. 2007b, 2009; Epinat et al. 2009; Jones et al. 2010; Lemoine-Busserolle et al. 2010; Wisnioski et al. 2011). Intensity weighting makes $\sigma_{\rm m}$ robust against errors from lower signal-to-noise ratio regions within the integral-field spectroscopy. The $\sigma_{\rm m}$ estimate of velocity dispersion is independent of any assumptions inherent in a parametric model of the galaxy kinematics, making it useful for galaxies that are not RD.

The quantity $\sigma_{\rm m}$ can be biased by velocity shear on scales smaller than the resolution element of the observation, as discussed by Davies et al. (2011). This effect, well known in radio astronomy as 'beam smearing,' can artificially inflate $\sigma_{\rm m}$ over the intrinsic velocity dispersion. In the extreme case of a galaxy with a strong velocity shear due to rapid rotation and observed with poor resolution, the effect renders $\sigma_{\rm m}$ useless as a measure of velocity dispersion. Correcting for beam smearing requires knowledge of the underlying velocity field at infinite resolution. For a well-understood velocity field, such as an RD, the unresolved velocity shear can be estimated using a model and removed from the observed velocity dispersion within each pixel, $\sigma_{\rm pix}$, before computing $\sigma_{\rm m}$. For a poorly understood velocity field, such as in a merger, it is not possible to remove the unresolved velocity shear because we do not know the underlying velocity field and how it affects $\sigma_{\rm m}$ through beam smearing. Alternately, fitting a disc model that includes velocity dispersion, as suggested by Davies et al., would also be invalid where the velocity field is not representative of a disc or if the intrinsic velocity dispersion was not constant.

In Green et al. (2010), we corrected for beam smearing using the *measured* velocity field. Davies et al. (2011) point out this is not strictly valid as the measured velocity field is already convolved with the point spread function. Given the spatial resolution of our data, we estimated this was a small effect except in the inner regions of each galaxy. In this paper, we provide an improved correction for beam smearing based on our best-fitting disc model. The disc model already accounts for beam smearing, avoiding including the effects of seeing twice. This correction is better in principle for disc galaxies, but is not applicable to non-disc velocity fields and so we do not apply it, as explained below. For such non-discs, we still compute (uncorrected) $\sigma_{\rm m}$, as it is meaningful for those classes of galaxies.

Our correction for beam smearing from disc rotation is applied to galaxies classified above as rotating as follows. First a map of unresolved velocity shear present in the best-fitting disc model is created using the prescription described in Appendix A. For this map, we assume the Hα intensity distribution is that of the exponential surface-brightness profile from SDSS. Then, this map of unresolved shear is subtracted in quadrature from the observed map of velocity dispersion (the observed map has already had instrumental broadening removed, Section 4.1). In the rare cases where the subtraction would produce an imaginary (non-physical) result, we have set the velocity dispersion to zero at that point in the resultant map. Finally, we compute $\sigma_{\rm m}$ from the resulting map.

The correction does not address beam smearing arising from sources other than the disc-like rotation of a galaxy. Consequently, we do not apply it to galaxies classified as CK or cCK. We have checked, using model data, that where the assumptions of surface brightness and rotation accurately represent the intrinsic velocity map of the galaxy, the correction fully removes any signature of beam smearing on the velocity dispersion of observed (beam smeared) data. For galaxies where these assumptions are not correct, observations with greater spatial resolution will be the best way to reduce the impact of beam smearing.

For our sample, the correction for beam smearing due to disc rotation does not qualitatively affect our results. The correction is typically small, with a median correction of 3.6 km s^{-1}, although in some cases (as expected for the most compact galaxies with the smallest dispersions) it can be much larger. Fig. 5 shows the amount by which $\sigma_{\rm m}$ is corrected by beam smearing due to disc rotation. The points are coded by their kinematic classification. Galaxies showing the clearest signatures of rotation (RD and cRD classifications, blue symbols) show the largest range in correction. Galaxies that do not show signatures of rotation (CK and cCK) have not been corrected and are not shown in Fig. 5. The galaxies C 13-3, C 20-2, D 21-3, B 14-1, A 4-3 and D 15-2 have the largest corrections, greater than 20 km s^{-1}. These galaxies have very low intrinsic velocity dispersions ($\sigma_{m,\rm corr} \lesssim 10\,{\rm km\,s^{-1}}$), unusually high concentrations, large circular velocities along the line of sight, or more typically some combination of the three. In any of these scenarios, the central region, which is most affected by beam smearing, tends to dominate in the computation of $\sigma_{\rm m}$.

Independent of the correction, we have obtained AO-corrected integral-field spectroscopy at 10 times higher spatial resolution for several of our galaxies as a further test of the potential effects of

[8] `expRad_r` in the `PhotoObj` view of the SDSS data base.

Downloaded from http://mnras.oxfordjournals.org/ at Liverpool John Moores University on October 27, 2016

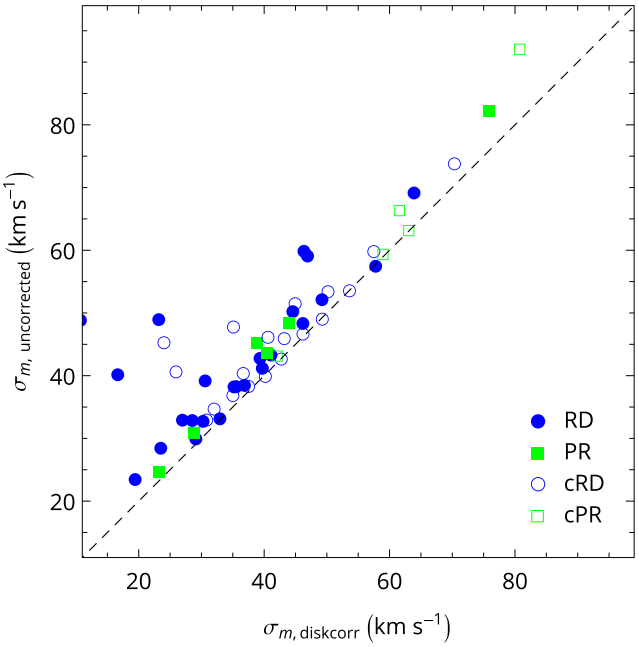

Figure 5. The effect of our correction method on the value of σ_{m}. The value after correcting for the velocity gradient based on our disc model and assuming an exponential surface-brightness profile is shown on the horizontal axis, while the raw σ_{m} before correction is shown on the vertical axis. The correction can only reduce the velocity dispersion, so points are only scattered above the one–one relation shown by the dashed line. The CK and cCK objects are not corrected (and not shown) because they do not match the assumptions of the correction.

beam smearing on σ_{m}. Those data show that beam smearing has a negligible effect on the value of σ_{m} for these galaxies.[9] We conclude that while beam smearing is present in our data, σ_{m}, particularly with this correction, remains a good relative indicator of velocity dispersion in the ionized gas of galaxies in our sample and the sample of Green et al. (2010).

5 RESULTS

5.1 Qualitative results from integral-field spectroscopy

We first make a few qualitative observations about the galaxies in our sample. The spatial maps of flux, relative velocity and velocity dispersion in gas emitting in the Hα line created from the integral-field spectroscopic data are included in the online data. Also shown with these maps are relevant physical quantities characterizing each galaxy, which we will discuss in more detail below. The velocity field of the best-fitting disc model is also shown, and the differences between the model velocities and the observed velocities.

A range of morphologies is seen in the maps of Hα emission. Roughly two-thirds of the galaxies in the sample show Hα emission that is centrally concentrated. This dominance of centrally concentrated star formation is unsurprising given much of the sample is effectively selected to have high Hα surface brightness in the central 3 arcsec. Our sample is unlikely to include galaxies with strong star formation only outside the central few arc-seconds of the galaxy, such as in large rings. Despite this bias, our sample does include galaxies with more complex Hα morphologies. Doubles, as well as galaxies with distributed, clumpy star formation are present. The complexity of the Hα spatial distributions make clear that a one- or two-component radial profile is inadequate to describe the Hα surface-brightness distributions in many of these galaxies – a common assumption when considering the disc-like nature of galaxies at any redshift. The distribution of Hα emission, and consequently of star formation, can be much more complex than the SDSS broad-band imaging reveals.

About half of the galaxies in our sample have regular, rotation-like symmetry. For comparison, in the largest sample observed with integral-field spectroscopy at high redshift, the SINS survey, approximately two-thirds of the galaxies are either compact, dispersion-dominated systems or mergers (Förster Schreiber et al. 2009). This high fraction of disturbed kinematics has been seen in other high-redshift surveys as well (Flores et al. 2006; Epinat et al. 2012). Interestingly, in our sample even some obvious mergers, such as E 0–3 and G 21–2 still show disc-like velocity fields within the individual merging galaxies. Also, many objects with complex, clumpy distributions of star formation do still show smooth rotation, such as D 14–1, C 13–1 and C 0–1. Genzel et al. (2011) and Wisnioski et al. (2012) have made similar arguments for $z > 1$ star-forming galaxies, where the star-forming clumps appear to be embedded in a disc-like velocity field.

5.2 Star formation rates

Total SFR of DYNAMO galaxies have been estimated from their Hα luminosities, after correcting for extinction due to interstellar dust. The Hα luminosities are measured by spatially integrating the Hα emission-line flux (regions masked during the emission-line fitting are excluded, Section 4.1).

The extinction correction was derived from the Balmer decrement using the method of Calzetti, Kinney & Storchi-Bergmann (1996) and Calzetti (1997). The observed flux ratio of Hα to Hβ was obtained from the MPA-JHU value-added catalogue fluxes (Tremonti et al. 2004). The mean extinction at Hα derived using this method for the galaxies in our sample is 1.0 mag.

The Balmer-decrement method for estimating dust extinction used here differs from that used in typical high-redshift analyses. For galaxies at high redshift, stellar-population models are fit to the spectral energy distribution (SED) of the galaxy, as direct measurements of both Hα and Hβ luminosity are difficult. Stellar-population fits provide estimates of dust attenuation, which can then be applied to emission-line fluxes used to estimate SFR. Argence & Lamareille (2009) explore whether these two methods provide comparable estimates of star formation. They find the dust corrections derived from SED fitting are not applicable for measuring SFR via emission-line fluxes. Therefore, quantitative comparisons between SFR in galaxies presented here and those of high-redshift galaxies should be treated cautiously.

The SFR was calculated from the extinction-corrected Hα luminosity using the conversion of Kennicutt (1998a) modified for a Chabrier (2003) IMF

$$\mathrm{SFR} = 0.56 L_{\mathrm{H}\alpha,\mathrm{int}} \left(7.9 \times 10^{-42} \frac{\mathrm{M}_\odot\ \mathrm{yr}^{-1}}{\mathrm{erg\ sec}^{-1}}\right). \quad (4)$$

The SFR for DYNAMO galaxies cover a broad range from 0.2 to 56.6 $\mathrm{M}_\odot\ \mathrm{yr}^{-1}$, with a median of 9.1 and a mean of 12.7 $\mathrm{M}_\odot\ \mathrm{yr}^{-1}$. For comparison, SINS galaxies at $z \simeq 2$ range from a few to over 100 $\mathrm{M}_\odot\ \mathrm{yr}^{-1}$ (but with the caveat about the method of correcting for dust extinction mentioned previously). Local galaxies in the

[9] We will present these data in detail in a future paper.

Downloaded from http://mnras.oxfordjournals.org/ at Liverpool John Moores University on October 27, 2016

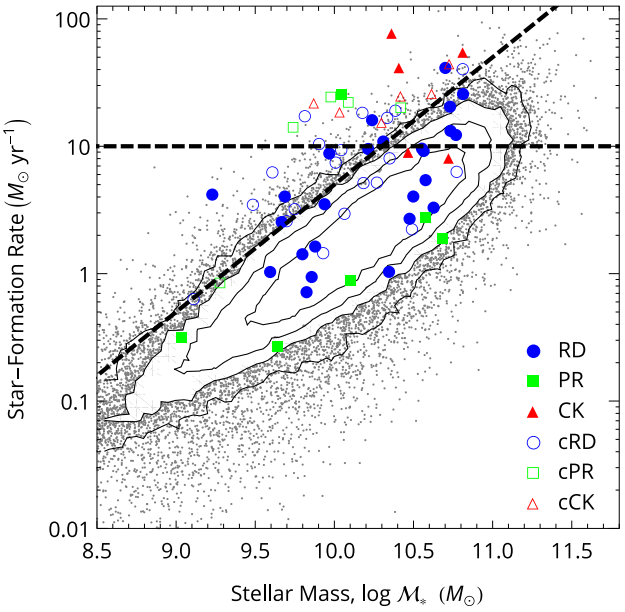

Figure 6. The coloured symbols show the SFR and stellar masses of the selected galaxies. The small grey points and logarithmic-density contours show the distribution of all star-forming galaxies from SDSS (classified as 'SF' by Brinchmann et al. 2004). Stellar masses for both are derived by Kauffmann et al. (2003b). Total (aperture-corrected) SFR for the broader SDSS sample are derived by Brinchmann et al. (2004), but for our sample the SFR derived in Section 5.2 are shown. Our estimates of the SFR correlate well with those of Brinchmann et al. (2004). The dashed lines show specific SFR of 5×10^{-10} yr^{-1} and SFR of 10 M$_\odot$ yr^{-1}. These limits are used to divide the galaxy sample in subsequent sections.

GHASP sample have SFR ranging from less than 0.1 M$_\odot$ yr^{-1} to about 10 M$_\odot$ yr^{-1}. The SFR of galaxies in our sample extend across both nearby star-forming galaxies and the typical galaxies studied at high redshifts (which have extreme SFR compared to local galaxies).

Fig. 6 shows the distribution of SFR and stellar masses for our sample overlaid on the whole of the star-forming sample of SDSS. The SFR shown for the SDSS galaxies are the aperture corrected values of Brinchmann et al. (2004). Unsurprisingly, the most disturbed galaxies, those classified as CK or cCK, tend to show the highest SFR because the disturbance has destabilized the gas reservoirs. Also shown in Fig. 6 are limits in specific SFR and SFR. We will use these limits in later sections for internal comparisons of our sample.

5.3 Total gas content

A large supply of gas is necessary to maintain high rates of star formation in galaxies for any significant period. Unfortunately, neutral and molecular gas reservoirs are difficult to detect with current telescopes even at $z \lesssim 0.1$ because the gas is either very diffuse or fairly cool, and consequently has low surface brightness. The relationship observed in local galaxies between the surface density of the rate of star formation, $\Sigma_{\rm SFR}$, and the total gas surface density, $\Sigma_{\rm gas}$, (the Kennicutt–Schmidt law, Kennicutt 1998b), has been used to infer the quantity of gas in galaxies at high redshift. Many of those galaxies have high gas fractions (Erb et al. 2006a; Förster Schreiber et al. 2009; Lemoine-Busserolle et al. 2010). We use this same empirical relationship to estimate the gas masses for the galaxies in our sample.

The star formation surface density is defined as the SFR per spatial pixel divided by the physical area covered by the pixel at the galaxy redshift. We have included a correction for the inclination of each galaxy as measured from the SDSS photometry. This correction may not be the best approach for galaxies classified as CK or those with a geometrically thick disc, where a volumetric law may be more appropriate (Krumholz, Dekel & McKee 2012). Equation 4 of Kennicutt (1998b) is used to estimate the total gas surface density (H I and H_2) per pixel, which then gives the total gas mass of the galaxy. Statistical error estimates include the 1σ confidence intervals of their equation 4. The conversions for SFR and the Kennicutt–Schmidt law are both based on the same IMF, making the gas masses computed independent of the IMF. Note also that the Kennicutt–Schmidt law is based on observed rates of star formation up to 1000 M$_\odot$ yr^{-1} kpc^{-2}, and therefore should remain valid even for the most extreme galaxies observed here. These masses are listed in Table 4. They range from 0.82 to 50×10^9 M$_\odot$, which is similar to the SINS survey mass range of 1.4 to 40×10^9 M$_\odot$ (Förster Schreiber et al. 2009).

The fraction of baryons in gas (by mass) is computed for each galaxy in the sample:

$$f_{\rm gas} \equiv \frac{\mathcal{M}_{\rm gas}}{(\mathcal{M}_{\rm gas} + \mathcal{M}_*)}. \quad (5)$$

We assume the total mass of baryons in each galaxy to be the sum of the gas mass and the stellar mass. The stellar masses used are those of Kauffmann et al. (2003a). Dust is also present, but makes up a negligible fraction of the mass of baryons. The estimated mass fraction of gas varies from 0.06 to 0.77 across our sample, as shown in Fig. 7. Higher gas fractions are found mostly in galaxies with SFR above a few M$_\odot$ yr^{-1}, although this may be a circular consequence of the dependence of our method for estimating the gas mass on SFR. Across the whole sample, the mass fraction of gas does not correlate with the gas velocity dispersion, $\sigma_{\rm m}$, or with the stellar mass of the galaxy (Pearson's $R = -0.42$ and 0.44, respectively). However, when only the galaxies with SFR below 10 M$_\odot$ yr^{-1} are considered, there is more correlation ($R = -0.68$), in agreement with Saintonge et al. (2011). At a given stellar mass, it is the galaxies forming stars at the highest rates that have the highest estimated gas mass fractions.

5.4 Tully–Fisher relation

We now plot the TFR for our sample to confirm our kinematic classification criteria and explore potential sources of evolution in the relation. Tully & Fisher (1977) report a relationship between circular velocity and luminosity (or mass) in disc galaxies. The TFR has become a key kinematic relationship for disc galaxies (Mathewson & Ford 1996; Courteau 1997; McGaugh et al. 2000; Verheijen 2001; Chiu, Bamford & Bunker 2007; Pizagno et al. 2007, etc.). Recent studies have argued for evolution in the TFR at higher redshift (Puech et al. 2008; Cresci et al. 2009; Gnerucci et al. 2011; Vergani et al. 2012) although there is also evidence against this (Miller et al. 2011, 2012). If part of our sample is really representative of high-redshift galaxies, then an offset in the TFR in that sub-sample may be apparent.

5.4.1 Tully–Fisher relation as a test kinematic classification

We compare galaxies in our sample to the TFR for disc galaxies to help demonstrate that part of the sample is indeed disc-like. In

Downloaded from http://mnras.oxfordjournals.org/ at Liverpool John Moores University on October 27, 2016

Table 4. Basic and star formation properties of the sample.

Sel. ID	z	M_r^a	$\mathcal{M}_*{}^b$ (10^9 M$_\odot$)	$L_{\rm fibre}$(Hα)^c (log erg s^{-1})	$L_{\rm IFU}$(Hα)^d (log erg s^{-1})	SFR$^e_{\rm B04}$ (M$_\odot$ yr^{-1})	SFR$^f_{\rm H\alpha}$ (M$_\odot$ yr^{-1})	Ext.^{g} (mag)	$\mathcal{M}^h_{\rm gas}$ (10^9 M$_\odot$)
A 04-3	0.069 07	− 21.2	42.35	40.18	$41.36^{+0.03}_{-0.03}$	1.78	$3.42^{+0.73}_{-0.73}$	$1.32^{+0.20}_{-0.25}$	6.89 ± 0.35
A 04-4	0.066 17	− 19.4	1.09	39.93	$40.88^{+0.04}_{-0.04}$	0.29	$0.33^{+0.05}_{-0.05}$	$-0.02^{+0.13}_{-0.14}$	1.08 ± 0.06
A 08-3	0.064 08	− 20.3	6.28	40.02	$41.16^{+0.02}_{-0.02}$	0.81	$1.47^{+0.29}_{-0.29}$	$0.92^{+0.19}_{-0.24}$	3.22 ± 0.13
A 08-4	0.059 21	− 20.7	48.53	40.04	$41.18^{+0.03}_{-0.03}$	3.66	$1.97^{+0.41}_{-0.41}$	$1.18^{+0.20}_{-0.24}$	3.15 ± 0.13
A 10-1	0.081 38	− 20.5	37.66	40.29	$41.02^{+0.03}_{-0.03}$	1.48	$2.86^{+0.59}_{-0.59}$	$1.99^{+0.20}_{-0.24}$	4.80 ± 0.35
A 10-2	0.061 83	− 19.8	12.56	40.10	$40.97^{+0.03}_{-0.03}$	0.59	$0.92^{+0.16}_{-0.16}$	$0.87^{+0.16}_{-0.19}$	1.78 ± 0.09
A 13-2	0.076 90	− 20.0	4.36	40.12	$40.88^{+0.02}_{-0.02}$	0.44	$0.28^{+0.04}_{-0.04}$	$-0.20^{+0.15}_{-0.18}$	0.96 ± 0.11
B 04-3	0.066 11	− 20.6	31.53	40.47	$41.40^{+0.04}_{-0.05}$	3.85	$4.18^{+0.59}_{-0.59}$	$1.46^{+0.10}_{-0.12}$	6.14 ± 0.28
B 04-4	0.075 55	− 20.5	11.58	40.63	$41.74^{+0.04}_{-0.05}$	2.00	$3.05^{+0.38}_{-0.38}$	$0.26^{+0.08}_{-0.08}$	6.35 ± 0.43
B 08-3	0.063 13	− 20.8	16.36	40.38	$41.85^{+0.04}_{-0.05}$	0.31	$9.87^{+1.54}_{-1.54}$	$1.26^{+0.12}_{-0.14}$	14.77 ± 0.42
B 08-4	0.055 97	− 20.1	4.65	40.26	$41.53^{+0.04}_{-0.05}$	0.68	$2.64^{+0.33}_{-0.33}$	$0.62^{+0.08}_{-0.09}$	4.19 ± 0.18
B 10-1	0.066 61	− 19.9	3.93	40.26	$41.16^{+0.02}_{-0.01}$	0.86	$1.07^{+0.14}_{-0.14}$	$0.57^{+0.13}_{-0.15}$	2.15 ± 0.10
B 11-2	0.075 33	− 20.3	8.67	40.32	$41.67^{+0.04}_{-0.05}$	3.05	$3.64^{+0.66}_{-0.66}$	$0.62^{+0.15}_{-0.18}$	9.10 ± 1.23
B 14-1	0.060 68	− 20.3	22.15	40.31	$40.86^{+0.02}_{-0.02}$	2.92	$1.07^{+0.10}_{-0.10}$	$1.33^{+0.08}_{-0.09}$	2.31 ± 0.16
B 15-1	0.065 75	− 20.4	6.67	40.22	$41.12^{+0.01}_{-0.01}$	1.11	$0.74^{+0.08}_{-0.08}$	$0.26^{+0.11}_{-0.12}$	1.93 ± 0.10
B 15-2	0.076 61	− 20.0	7.19	40.33	$41.07^{+0.02}_{-0.02}$	0.72	$0.98^{+0.14}_{-0.14}$	$0.69^{+0.14}_{-0.16}$	1.66 ± 0.12
B 20-1	0.080 17	− 20.8	7.56	40.51	$41.40^{+0.01}_{-0.01}$	1.01	$1.69^{+0.17}_{-0.17}$	$0.48^{+0.10}_{-0.10}$	4.07 ± 0.33
C 00-1	0.060 83	− 19.5	1.29	40.77	$41.29^{+0.01}_{-0.01}$	0.39	$0.65^{+0.04}_{-0.04}$	$-0.29^{+0.05}_{-0.06}$	1.35 ± 0.08
C 04-1	0.066 57	− 20.0	4.86	40.74	$41.65^{+0.04}_{-0.05}$	1.18	$4.18^{+0.48}_{-0.48}$	$0.82^{+0.06}_{-0.06}$	5.94 ± 0.32
C 04-2	0.070 67	− 19.9	3.06	40.71	$41.64^{+0.04}_{-0.05}$	1.31	$3.59^{+0.41}_{-0.41}$	$0.69^{+0.06}_{-0.06}$	4.94 ± 0.31
C 13-1	0.078 76	− 21.7	35.78	40.72	$41.94^{+0.01}_{-0.01}$	4.03	$9.93^{+0.93}_{-0.93}$	$1.05^{+0.09}_{-0.10}$	14.22 ± 1.02
C 13-3	0.071 10	− 20.8	37.71	40.78	$41.41^{+0.01}_{-0.01}$	3.97	$5.62^{+0.50}_{-0.50}$	$1.74^{+0.09}_{-0.10}$	5.94 ± 0.48
C 14-2	0.056 20	− 20.2	5.61	40.78	$41.49^{+0.01}_{-0.01}$	0.63	$3.32^{+0.17}_{-0.17}$	$0.98^{+0.05}_{-0.05}$	3.88 ± 0.29
C 20-2	0.077 22	− 20.2	8.50	40.67	$41.29^{+0.02}_{-0.02}$	0.75	$1.50^{+0.13}_{-0.13}$	$0.61^{+0.08}_{-0.08}$	2.72 ± 0.21
C 21-1	0.078 50	− 21.1	30.92	40.72	$41.17^{+0.03}_{-0.03}$	3.97	$2.30^{+0.32}_{-0.32}$	$1.37^{+0.12}_{-0.14}$	3.63 ± 0.45
C 22-2	0.071 16	− 21.0	15.28	41.05	$41.68^{+0.01}_{-0.01}$	4.89	$5.32^{+0.28}_{-0.28}$	$1.00^{+0.05}_{-0.05}$	7.24 ± 0.55
D 00-2	0.081 30	− 21.6	24.30	41.59	$42.21^{+0.01}_{-0.01}$	9.86	$19.65^{+0.72}_{-0.72}$	$1.11^{+0.04}_{-0.04}$	18.74 ± 1.74
D 10-4	0.067 38	− 20.3	5.49	41.53	$42.24^{+0.01}_{-0.01}$	5.43	$14.66^{+0.55}_{-0.55}$	$0.70^{+0.03}_{-0.03}$	13.80 ± 0.89
D 13-1	0.058 81	− 20.0	1.69	41.08	$41.85^{+0.01}_{-0.01}$	1.29	$4.33^{+0.17}_{-0.17}$	$0.36^{+0.04}_{-0.04}$	5.17 ± 0.33
D 13-5	0.075 35	− 21.7	53.84	41.52	$42.10^{+0.01}_{-0.01}$	15.14	$21.20^{+0.86}_{-0.86}$	$1.46^{+0.04}_{-0.04}$	20.17 ± 1.48
D 14-1	0.073 62	− 21.0	20.37	41.24	$41.92^{+0.01}_{-0.01}$	6.51	$11.30^{+0.54}_{-0.54}$	$1.23^{+0.05}_{-0.05}$	17.46 ± 8.76
D 15-1	0.059 29	− 19.8	4.99	40.96	$41.45^{+0.02}_{-0.02}$	0.96	$2.67^{+0.17}_{-0.17}$	$0.83^{+0.05}_{-0.05}$	3.00 ± 0.29
D 15-2	0.056 19	− 19.1	1.89	40.97	$41.22^{+0.02}_{-0.02}$	0.76	$0.88^{+0.06}_{-0.06}$	$0.21^{+0.04}_{-0.04}$	1.17 ± 0.15
D 15-3	0.067 12	− 21.4	54.15	41.03	$41.79^{+0.01}_{-0.01}$	7.69	$13.70^{+1.00}_{-1.00}$	$1.77^{+0.07}_{-0.08}$	14.74 ± 0.88
D 20-1	0.070 49	− 20.9	18.56	41.22	$41.74^{+0.01}_{-0.01}$	5.63	$5.35^{+0.25}_{-0.25}$	$0.88^{+0.05}_{-0.05}$	6.80 ± 0.55
D 21-3	0.057 46	− 21.2	29.87	41.05	$41.40^{+0.01}_{-0.01}$	6.10	$2.80^{+0.18}_{-0.18}$	$1.02^{+0.06}_{-0.07}$	3.29 ± 0.32
D 22-1	0.067 93	− 21.9	59.24	41.06	$41.78^{+0.01}_{-0.01}$	6.74	$6.51^{+0.45}_{-0.45}$	$0.98^{+0.07}_{-0.07}$	9.90 ± 1.13
D 22-2	0.081 21	− 20.8	9.29	41.27	$41.91^{+0.01}_{-0.01}$	5.10	$9.11^{+0.37}_{-0.37}$	$1.02^{+0.04}_{-0.04}$	11.64 ± 0.71
D 23-1	0.080 89	− 21.1	10.20	41.34	$41.83^{+0.01}_{-0.01}$	3.83	$7.69^{+0.35}_{-0.35}$	$1.02^{+0.05}_{-0.05}$	8.42 ± 0.74
E 00-2	0.145 77	− 21.7	29.19	41.66	$41.97^{+0.01}_{-0.01}$	10.61	$9.27^{+0.32}_{-0.32}$	$0.90^{+0.02}_{-0.03}$	8.03 ± 2.44
E 00-3	0.146 62	− 22.2	52.58	41.28	$41.84^{+0.01}_{-0.01}$	6.84	$8.35^{+0.54}_{-0.54}$	$1.09^{+0.06}_{-0.07}$	12.35 ± 1.46
E 04-1	0.149 97	− 21.7	58.67	41.49	$41.93^{+0.02}_{-0.02}$	10.25	$12.71^{+0.98}_{-0.98}$	$1.33^{+0.07}_{-0.07}$	19.10 ± 4.95
E 09-1	0.138 92	− 21.7	36.67	41.20	$41.90^{+0.02}_{-0.02}$	3.08	$9.53^{+0.98}_{-0.98}$	$1.10^{+0.10}_{-0.11}$	16.65 ± 8.94
E 10-1	0.138 97	− 22.0	65.00	41.52	$42.23^{+0.01}_{-0.01}$	28.08	$26.66^{+1.73}_{-1.73}$	$1.39^{+0.06}_{-0.06}$	31.96 ± 6.23
E 23-1	0.144 85	− 21.5	19.82	41.69	$42.20^{+0.01}_{-0.01}$	4.92	$15.99^{+0.76}_{-0.76}$	$0.91^{+0.04}_{-0.04}$	23.04 ± 3.27
F 08-2	0.064 75	− 20.7	7.40	41.80	$42.47^{+0.04}_{-0.05}$	8.61	$22.66^{+2.36}_{-2.36}$	$0.60^{+0.03}_{-0.03}$	19.35 ± 1.31
F 09-1	0.082 79	− 21.0	22.95	41.77	$42.63^{+0.04}_{-0.05}$	25.05	$79.79^{+8.40}_{-8.40}$	$1.58^{+0.04}_{-0.04}$	49.12 ± 4.53
F 10-1	0.083 51	− 20.4	4.06	41.58	$42.06^{+0.04}_{-0.05}$	2.00	$6.44^{+0.69}_{-0.69}$	$0.26^{+0.04}_{-0.04}$	18.60 ± ∞^i
F 12-4	0.067 28	− 21.6	15.03	41.54	$42.42^{+0.04}_{-0.05}$	8.90	$18.91^{+1.99}_{-1.99}$	$0.53^{+0.04}_{-0.04}$	21.29 ± 1.12
G 03-2	0.129 46	− 21.3	6.51	41.81	$42.37^{+0.01}_{-0.01}$	7.91	$17.79^{+0.89}_{-0.89}$	$0.59^{+0.05}_{-0.05}$	28.43 ± 7.93

Downloaded from http://mnras.oxfordjournals.org/ at Liverpool John Moores University on October 27, 2016

Table 4 – *continued*

Sel. ID	z	M_r^a	$\mathcal{M}_*{}^b$ (10^9 M$_\odot$)	$L_{\rm fibre}$(Hα)^c (log erg s^{-1})	$L_{\rm IFU}$(Hα)^d (log erg s^{-1})	SFR$^e_{\rm B04}$ (M$_\odot$ yr^{-1})	SFR$^f_{\rm H\alpha}$ (M$_\odot$ yr^{-1})	Ext.^{g} (mag)	$\mathcal{M}^h_{\rm gas}$ (10^9 M$_\odot$)
G 03-4	0.133 73	−21.4	64.61	41.84	$42.35^{+0.01}_{-0.01}$	41.03	$56.62^{+2.08}_{-2.08}$	$1.90^{+0.03}_{-0.03}$	52.90 ± 6.61
G 04-1	0.129 81	−22.0	64.74	41.75	$42.36^{+0.01}_{-0.01}$	28.04	$41.61^{+2.17}_{-2.17}$	$1.55^{+0.05}_{-0.05}$	43.68 ± 11.65
G 08-1	0.134 92	−21.2	8.01	41.77	$42.26^{+0.01}_{-0.01}$	5.98	$10.77^{+0.38}_{-0.38}$	$0.31^{+0.03}_{-0.03}$	36.76 ± ∞^i
G 08-2	0.131 94	−21.2	41.09	41.67	$42.13^{+0.01}_{-0.01}$	19.24	$26.85^{+1.67}_{-1.67}$	$1.64^{+0.06}_{-0.06}$	30.12 ± 8.59
G 08-3	0.142 70	−21.6	25.54	41.91	$42.57^{+0.01}_{-0.01}$	10.56	$42.84^{+1.80}_{-1.80}$	$1.04^{+0.04}_{-0.04}$	44.83 ± 4.25
G 08-4	0.139 64	−21.5	11.05	41.71	$42.12^{+0.01}_{-0.01}$	5.65	$9.65^{+0.54}_{-0.54}$	$0.55^{+0.05}_{-0.05}$	16.29 ± 4.94
G 08-5	0.132 17	−21.2	17.31	41.69	$42.05^{+0.01}_{-0.01}$	9.77	$16.62^{+1.02}_{-1.02}$	$1.31^{+0.05}_{-0.06}$	23.60 ± 4.96
G 09-1	0.139 96	−21.5	26.13	41.77	$42.18^{+0.01}_{-0.01}$	11.96	$25.70^{+1.47}_{-1.47}$	$1.46^{+0.05}_{-0.05}$	33.42 ± 9.57
G 10-1	0.143 72	−21.7	12.24	41.92	$42.37^{+0.01}_{-0.01}$	9.64	$23.00^{+1.00}_{-1.00}$	$0.87^{+0.04}_{-0.04}$	28.39 ± 3.21
G 11-1	0.137 05	−22.5	50.27	41.78	$42.46^{+0.01}_{-0.01}$	20.23	$42.74^{+2.05}_{-2.05}$	$1.33^{+0.05}_{-0.05}$	46.67 ± 14.12
G 13-1	0.138 76	−21.7	11.11	42.21	$42.58^{+0.01}_{-0.01}$	24.54	$26.47^{+0.78}_{-0.78}$	$0.50^{+0.03}_{-0.03}$	24.09 ± 2.78
G 14-1	0.132 33	−21.7	22.33	41.69	$41.93^{+0.01}_{-0.01}$	10.11	$8.30^{+0.33}_{-0.33}$	$0.86^{+0.04}_{-0.04}$	9.72 ± 2.38
G 14-3	0.144 64	−21.4	26.27	41.94	$42.16^{+0.01}_{-0.01}$	19.98	$20.87^{+0.95}_{-0.95}$	$1.30^{+0.04}_{-0.05}$	18.44 ± 4.33
G 20-1	0.132 77	−22.0	53.06	42.30	$42.63^{+0.00}_{-0.00}$	26.65	$46.03^{+1.23}_{-1.23}$	$0.98^{+0.03}_{-0.03}$	33.72 ± 5.43
G 20-2	0.141 13	−22.0	21.56	41.91	$42.26^{+0.01}_{-0.01}$	19.16	$17.27^{+0.66}_{-0.66}$	$0.83^{+0.04}_{-0.04}$	19.12 ± 4.16
G 21-2	0.134 99	−21.1	10.78	41.76	$42.21^{+0.01}_{-0.01}$	9.83	$19.26^{+0.95}_{-0.95}$	$1.07^{+0.05}_{-0.05}$	29.25 ± 35.03
H 10-2	0.149 07	−22.1	9.50	42.02	$42.68^{+0.04}_{-0.05}$	12.48	$25.35^{+2.68}_{-2.68}$	$0.21^{+0.04}_{-0.04}$	30.28 ± 2.73

[a]The r-band absolute magnitude.
[b]The stellar mass of the object reproduced from Kauffmann et al. (2003a). Their masses have been scaled by 0.88 to convert from their Kroupa (2001) initial mass function.
[c]The Hα luminosity as measured by the Sloan spectro-photometry from a 3 arcsec diameter fibre aperture.
[d]The Hα luminosity as measured by our IFU observations in the masked region (Section 4.1).
[e]The star formation rate reported by Brinchmann et al. (2004). These have been scaled by 0.88 to convert from their Kroupa (2001) initial mass function.
[f]The star formation rate measured from our IFU observations, including a dust correction (Section 5.2).
[g]The extinction of Hα due to dust in magnitudes.
[h]The gas mass (Section 5.3).
[i]These values are effectively unconstrained because of the inclination correction.

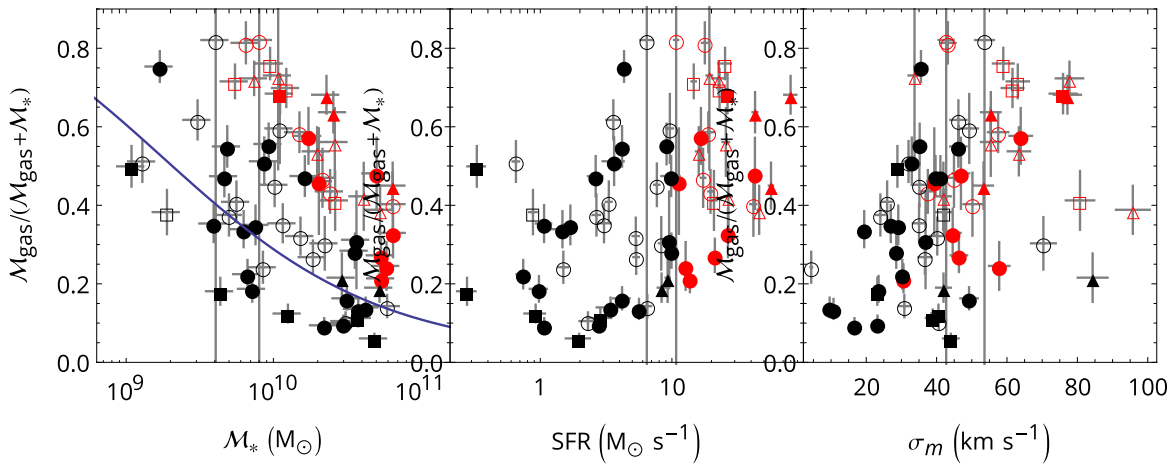

Figure 7. The estimated gas mass fraction for galaxies in our sample is shown as a function of stellar mass ($\mathcal{M}_*$), SFR and mean local velocity dispersion ($\sigma_{\rm m}$). The symbol shapes are coded by the kinematic classification (Section 4.3). The red symbols correspond to galaxies with SFR greater than 10 M$_\odot$ yr^{-1}, and the black symbols to those with lower SFR. (A cut on specific SFR roughly corresponds to gas fractions of 0.4, a simple reflection of the method used to compute the fractions.) Gas fractions have been estimated using the Kennicutt–Schmidt law, and so are not independent of the SFR. The smooth curve in the left-hand panel is the relationship between gas fraction and stellar mass found in the COLD GASS Survey (Saintonge et al. 2011). Error bars show statistical, 1σ errors for all quantities.

Downloaded from http://mnras.oxfordjournals.org/ at Liverpool John Moores University on October 27, 2016

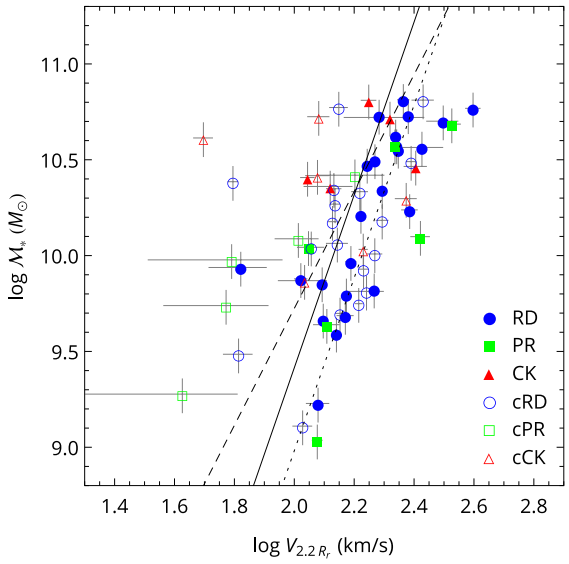

Figure 8. Stellar mass ($\mathcal{M}_*$, Kauffmann et al. 2003a) of galaxies in our sample plotted as a function of circular velocity ($V_{2.2R_r}$). Points are coded by their kinematic classification as shown at the lower right (Section 4.3). The circular velocity, $V_{2.2R_r}$ is inferred at 2.2 times the exponential disc scale radius in r-band, $2.2R_r$, using the best-fitting disc model (Section 4.4). For galaxies with complex kinematics (CK and cCK), $v_{\rm shear}/2$ is shown in place of $V_{2.2R_r}$ (Section 5.4). These CK objects (red triangles) do not show a correlation, while more disc-like galaxies correlate as expected (Tully & Fisher 1977). The local TFRs of Bell & de Jong (2001, solid line) and Pizagno et al. (2005, dashed line) are shown for comparison. The dotted line shows the offset relation found by Cresci et al. (2009) for $z \simeq 2$ galaxies. Statistical, 1σ error bars are included, but do not include any differences between the photometric and kinematic inclination.

general, galaxies that are not RD deviate from the relationship, usually towards lower circular velocities as the action of merging will convert systematic rotational motions to random ones and reduce overall velocity gradients (Covington et al. 2010). Observations with limited seeing of two galaxies merging could show a velocity field similar to that of aN RD, but are less likely to agree with the TFR. Consequently, we can use the TFR as a discriminator between galaxies with disc-like kinematics and those with velocity shear arising from other sources (such as mergers), and check that our kinematic classifications as e.g., RD and CK (Section 4.3) are valid.

The TFR for galaxies in our sample is shown in Fig. 8. The coloured symbols show the positions of galaxies in our sample, with the shape and colour of the symbol corresponding to its kinematic morphology derived in Section 4.3. Stellar masses for our galaxies have been determined by Kauffmann et al. (2003a), and are adjusted by a factor of 0.88 to account for the difference in IMF. We adopt circular velocities from disc fitting (Section 4.4) or, where those fits are not valid (e.g., CK and cCK classifications), from an estimate, $V_{\rm shear}/2$, of the maximum velocity shear across the galaxy. The velocity $V_{\rm shear}$ is the difference between the 5th percentile and the 95th percentile velocities observed in the velocity map (similar to Law et al. 2007b; Gonçalves et al. 2010; Wisnioski et al. 2011). This difference reflects the total velocity shear across the velocity map, while avoiding outliers in the distribution of velocities within the map. $V_{\rm shear}/2$ has been used in place of $V_{2.2R_r}$ for CK- and cCK-classified galaxies in Fig. 8 and is listed in parenthesis in the $V_{2.2R_r}$ column of Table 5. Not shown are galaxies with inclinations of less than 12° because the inclination correction introduces a large error to such systems.

The correlation with the TFR (or lack thereof) matches expectations from the kinematic morphology of galaxies within our sample. Galaxies classified as having CK (those with CK and cCK designations) are clearly offset to the left in Fig. 8, show almost no correlation (Pearson's $R = 0.06$), and do not follow the TFR. Some compact, disc-like galaxies (cRD and cPR) are also scattered to the left in Fig. 8. However, this apparent disagreement could be due to observational effects, as the atmospheric seeing can reduce modelled circular velocity as the angular size of a galaxy approaches the seeing limit (Epinat et al. 2010). Also, seeing can affect the estimate of inclination for a galaxy that is poorly resolved. Therefore, the comparison with the TFR does not confirm or reject cRD or cPR galaxies as disc-like, although they are better correlated ($R = 0.55$) than galaxies with CK. However, the remaining RD and PR classified galaxies do have correlated circular velocities and masses (Pearson's correlation coefficient of $R = 0.73$). The TFR confirms that the 25 RD and 6 PR classified galaxies are indeed discs.

The local TFRs of Bell & de Jong (2001) and Pizagno et al. (2005) are also shown in Fig. 8 for comparison (adjusted to a Chabrier 2003 IMF). There is still some disagreement between these two as to the exact slope of the local TFR (and in general, see Hammer et al. 2007 and Glazebrook 2013 for more discussion). Also apparent is that many of the DYNAMO galaxies have lower stellar masses than is typical for local galaxies of a fixed rotation velocity. We have already noted (Section 5.3) that many of these galaxies are extremely gas-rich, and high gas content can offset galaxies to higher circular velocities in the stellar mass TFR McGaugh et al. (2000); McGaugh (2005). Therefore, the disagreement between rotating galaxies in our sample and the local stellar mass TFR is not unexpected.

The RD and PR galaxies in our sample are compared with the baryonic TFR of McGaugh et al. (2000) for local galaxies in Fig. 9 (also adjusted to a Chabrier 2003 IMF). The positions of other galaxies in our sample are also shown. The trimmed sample agrees very well with the reference relation, further confirming that these galaxies host regular RD. Residual scatter is 0.5 dex rms in total mass for the galaxies classified as RD or PR. Including the gas mass for these galaxies brings them into agreement with the local TFR, further supporting their gas-rich nature.

5.4.2 *Evolution in the Tully–Fisher relation*

We compare rotating galaxies in our sample with two recent reports of evolution in the TFR at higher redshifts. While we would not expect to see any redshift evolution of the TFR in our sample, if the offset at high redshifts is a result of changes in star formation or gas velocity dispersion then it may also be apparent in our sample. Fig. 8 shows the 'evolved' relation of Cresci et al. (2009) for SINS survey galaxies at $z \simeq 2$ as a dotted line in addition to the local reference relations introduced above. Puech et al. (2008) also see an offset of the same scale as Cresci et al. for the IMAGES galaxies at $z \simeq 0.6$. However, when the mass in gas is included for gas-rich DYNAMO discs, they do not show a significant offset, as seen in Fig. 9. This result is also found in IMAGES (Puech et al. 2010) and in MASSIV (Vergani et al. 2012).

The rotating galaxies in our sample can be divided into two groups based on their specific SFR to check for any change in the TFR within our sample. Fig. 10 shows this division. The red symbols correspond to galaxies in our sample with specific SFR greater than $5 \times 10^{-10}\,{\rm yr}^{-1}$ (reflecting the position of the star formation main sequence at high redshift, Noeske et al. 2007), while the galaxies shown by the black symbols have lower specific SFR (more comparable to typical local disc galaxies). The red symbols show

Downloaded from http://mnras.oxfordjournals.org/ at Liverpool John Moores University on October 27, 2016

Table 5. Kinematic properties of the sample.

Sel. ID	$r_{\mathrm{petro},\,r}$ (kpc)	$r_{\mathrm{exp},\,r}$ (kpc)	r_t (kpc)	i	$V^a_{2.2R_r}$ (km s^{-1})	σ^b_{m} (km s^{-1})	Kinematic Class
A 04-3	9.8	4.9	0.7 ± 0.2	58	218 ± 2	10	RD
A 04-4	11.4	6.2	2.8 ± 0.1	54	119 ± 4	29	PR
A 08-3	10.7	5.9	2.6 ± 0.0	59	149 ± 3	19	RD
A 08-4	13.0	7.5	17.0 ± 0.1	80	336 ± 23	44	PR
A 10-1	10.7	7.2	2.5 ± 0.1	76	217 ± 3	39	PR
A 10-2	10.4	7.4	17.7 ± 0.1	81	264 ± 19	41	PR
A 13-2	13.4	5.6	3.7 ± 0.2	35	128 ± 12	23	PR
B 04-3	8.8	5.2	4.0 ± 0.2	69	186 ± 4	49	RD
B 04-4	6.8	2.9	1.8 ± 0.2	28	139 ± 11	35	cRD
B 08-3	10.2	6.5	3.6 ± 0.0	63	167 ± 2	40	RD
B 08-4	6.0	3.8	1.7 ± 0.1	56	125 ± 3	41	RD
B 10-1	7.1	4.7	2.7 ± 0.1	66	138 ± 4	27	RD
B 11-2	8.5	3.3	3.9 ± 0.0	20	66 ± 14	33	RD
B 14-1	8.3	5.9	0.6 ± 0.1	78	197 ± 2	17	RD
B 15-1	9.2	5.6	2.5 ± 0.1	44	185 ± 6	30	RD
B 15-2	11.0	5.4	1.4 ± 0.1	55	124 ± 3	24	RD
B 20-1	10.5	5.2	2.3 ± 0.1	35	105 ± 5	29	RD
C 00-1	6.3	3.0	2.9 ± 0.1	56	107 ± 8	32	cRD
C 04-1	6.4	3.5	3.9 ± 0.3	49	148 ± 9	46	RD
C 04-2	5.0	2.7	4.2 ± 0.6	59	65 ± 7	46	cRD
C 13-1	10.8	5.3	2.3 ± 0.1	31	223 ± 8	29	RD
C 13-3	8.1	5.1	0.7 ± 0.2	72	220 ± 2	11	RD
C 14-2	4.5	2.7	0.8 ± 0.0	58	164 ± 4	26	cRD
C 20-2	5.1	2.6	0.9 ± 0.1	45	170 ± 6	4	cRD
C 21-1	4.5	1.9	0.7 ± 0.2	58	246 ± 9	41	cRD
C 22-2	6.8	2.8	1.5 ± 0.1	35	197 ± 9	40	cRD
D 00-2	6.3	2.8	1.1 ± 0.1	35	62 ± 2	38	cRD
D 10-4	5.4	2.8	19.1 ± 0.2	68	59 ± 23	63	cPR
D 13-1	6.2	3.6	4.8 ± 0.1	76	120 ± 10	36	RD
D 13-5	9.0	4.4	0.7 ± 0.2	49	192 ± 2	46	RD
D 14-1	10.3	4.3	–	12	–	39	RD
D 15-1	4.0	2.0	0.6 ± 0.1	55	142 ± 5	24	cRD
D 15-2	2.4	0.6	0.5 ± 0.1	38	42 ± 22	42	cPR
D 15-3	8.9	4.7	0.8 ± 0.0	47	240 ± 3	31	RD
D 20-1	6.1	2.9	1.3 ± 0.0	39	137 ± 5	37	cRD
D 21-3	10.9	4.2	0.5 ± 0.1	57	175 ± 2	23	RD
D 22-1	5.2	2.0	0.6 ± 0.2	20	141 ± 10	31	cRD
D 22-2	9.1	5.0	5.5 ± 0.1	54	155 ± 6	35	RD
D 23-1	5.7	3.0	2.8 ± 0.1	54	186 ± 10	35	cRD
E 00-2	7.9	3.4	–	36	(127)	84	CK
E 00-3	19.6	7.4	–	64	(104)	42	CK
E 04-1	8.2	3.5	1.3 ± 0.3	35	395 ± 22	58	RD
E 09-1	8.8	4.2	1.6 ± 0.2	19	267 ± 46	37	RD
E 10-1	9.6	3.9	1.2 ± 0.3	31	231 ± 10	45	RD
E 23-1	7.4	2.6	–	44	(118)	63	cCK
F 08-2	3.7	1.8	–	65	(54)	78	cCK
F 09-1	7.5	3.7	–	62	(66)	77	CK
F 10-1	3.3	1.1	–	1	–	54	cRD
F 12-4	4.3	1.9	0.6 ± 0.2	35	134 ± 4	57	cRD
G 03-2	7.0	2.8	1.1 ± 0.3	24	174 ± 24	43	cRD
G 03-4	9.7	4.5	–	58	(89)	53	CK
G 04-1	8.2	3.1	1.2 ± 0.1	24	269 ± 22	50	cRD
G 08-1	6.3	1.6	–	1	–	43	cRD
G 08-2	5.8	1.9	–	29	(25)	42	cCK
G 08-3	8.6	4.2	–	52	(55)	55	CK
G 08-4	8.2	2.6	1.6 ± 0.2	30	114 ± 11	49	cRD
G 08-5	8.3	3.1	1.2 ± 0.1	36	243 ± 15	64	RD
G 09-1	6.8	2.7	–	29	(60)	55	cCK
G 10-1	6.2	2.5	6.1 ± 0.7	49	103 ± 17	62	cPR
G 11-1	9.7	4.3	2.8 ± 0.3	23	314 ± 37	47	RD
G 13-1	7.4	3.2	1.2 ± 0.3	69	112 ± 2	76	PR
G 14-1	7.1	2.5	1.2 ± 0.3	35	136 ± 8	70	cRD
G 14-3	5.5	1.6	3.9 ± 0.5	41	159 ± 40	81	cPR

Downloaded from http://mnras.oxfordjournals.org/ at Liverpool John Moores University on October 27, 2016

Table 5 – *continued*

Sel. ID	$r_{\rm petro,\,r}$ (kpc)	$r_{\rm exp,\,r}$ (kpc)	r_t (kpc)	i	$V^a_{2.2R_r}$ (km s^{-1})	$\sigma^b_{\rm m}$ (km s^{-1})	Kinematic Class
G 20-1	5.8	2.4	–	43	(60)	96	cCK
G 20-2	5.7	2.0	1.2 ± 0.3	34	166 ± 10	45	cRD
G 21-2	6.5	2.5	–	15	(85)	34	cCK
H 10-2	7.4	2.7	21.8 ± 3.3	49	62 ± 29	59	cPR

[a] For objects classified as CK and cCK, the value of $V_{\rm shear}/2$ is shown in parenthesis instead of $V_{2.2R_r}$.
[b] The statistical error on $\sigma_{\rm m}$ is typically 1–2 km s^{-1} (see Section 4.5).

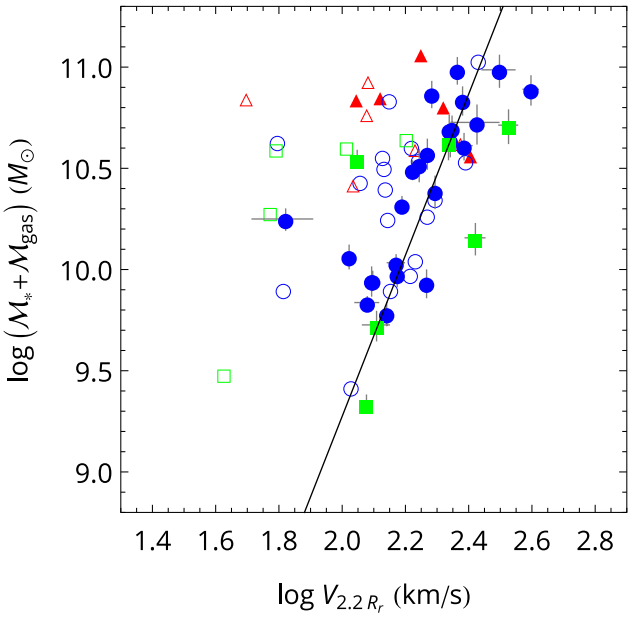

Figure 9. The baryonic TFR for the DYNAMO sample. Galaxies from the sample are plotted as in Fig. 8, but galaxies classified as rotating discs (RD and PR) have been highlighted. The error bars are omitted from the other points for clarity. The local baryonic TFR of McGaugh et al. (2000) is shown by the solid line and agrees well for the RD galaxies. Comparing with Fig. 8, it is apparent that the offset from the stellar mass TFR results from the high gas fractions inferred for many of the galaxies in our sample. The RD classified galaxy B 11-2 shows much lower circular velocity than expected; this galaxy is very round in appearance – the photometric inclination may not accurately reflect the kinematic inclination.

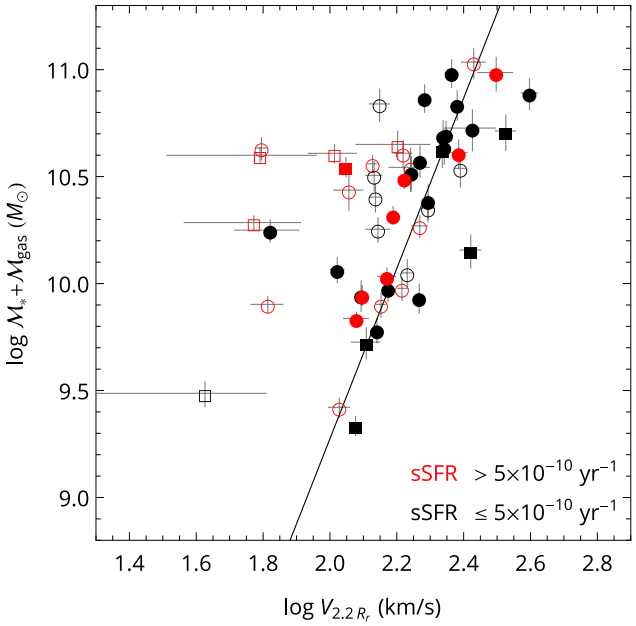

Figure 10. The impact of specific SFR on the TFR. Red symbols correspond to galaxies in our sample with specific SFR greater than 5×10^{-10} yr^{-1}, black symbols correspond to those with lesser specific SFR. The symbol shape corresponds to kinematic classification as in Fig. 8. The solid line shows the same local TFR of Bell & de Jong (2001) shown in Fig. 9. The galaxies with high specific SFR that are expected to be most similar to galaxies at high redshift show no systematic offset from more typical low-redshift galaxies.

no systematic offset to higher circular velocities than the rest of our sample. Instead, many of these galaxies scatter to lower circular velocities than local galaxies, although the compactness of some galaxies complicates our estimate of their circular velocities. In our sample, the TFR of RD galaxies with high specific SFR, which place them off the local star-formation main sequence, is indistinguishable from the TFR for RD galaxies lying on the main sequence.

We have divided our sample using several other properties to check for possible systematic differences. A division by SFR of 10 M$_\odot$ yr^{-1}, corresponding roughly to Hα luminosities of 10^{42} erg s^{-1}, reveals no offset. Similarly, dividing the sample by gas velocity dispersion, $\sigma_{\rm m}$, around 40 km s^{-1}, also does not reveal any clear offset or deviation from the local relation. While we cannot rule out true redshift evolution in the TFR, there is no evidence for evolution due to differences in total SFR, specific SFR or velocity dispersion, several of the primary differences observed between local and high-redshift galaxies. The stellar mass TFR is offset for galaxies that are gas rich. However, the baryonic TFR remains constant. Our conclusion is similar to that of Puech et al. (2010) and (Vergani et al. 2012), namely that the offset in the TFR claimed by e.g., Cresci et al. and Puech et al. (2008) reflects the gas richness of the samples concerned.

5.5 Disc stability and velocity dispersions

Genzel et al. (2011) presents a simple argument relating V/σ to gas mass fraction $f_{\rm gas}$. If one assumes that a gas disc is marginally stable (Toomre $Q \sim 1$) then one can derive:

$$\frac{V}{\sigma} \simeq \frac{a}{f_{\rm gas}}, \qquad (6)$$

where a is a numerical factor of value $1 < a < 2$ that depends on the shape of the disc's rotation curve. The Genzel et al. argument implies that gas fraction will correlate with the disc dynamical temperature (parametrized by σ) for marginally stable discs at a fixed mass (circular velocity, V, correlates with total mass, not gas fraction). Fig. 11 shows the parameter space of the stability criterion.

Downloaded from http://mnras.oxfordjournals.org/ at Liverpool John Moores University on October 27, 2016

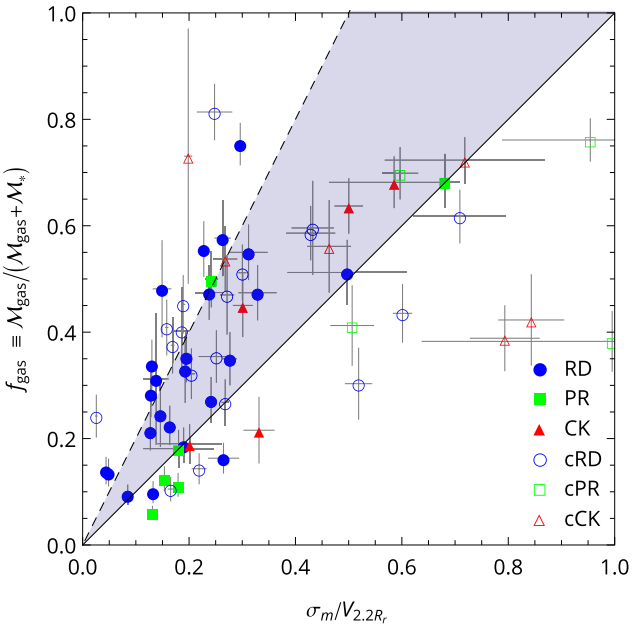

Figure 11. Gas fraction ($f_{\rm gas}$) as a function of the ratio σ/V for DYNAMO galaxies. The velocities are those used for our TFR analysis (Section 5.4). Lines show the stability limits for $a = 1$ (solid) and $a = 2$ (dashed).

A correlation, with Pearson's $R = 0.60$, between $\sigma_{\rm m}/V_{2.2R_r}$ and $f_{\rm gas}$ for disc-like galaxies (i.e., RD, cRD, PR and cPR classifications) is apparent. This correlation improves to $R = 0.69$ if only RD and PR classified galaxies are considered. Of these disc-like galaxies, 72 per cent fall in the region bounded by $a \geq 1$, the lower limit for disc stability, and this fraction rises to 81 per cent for the higher quality discs (RD and cRD classifications). We conclude that most of these galaxies are at least marginally stable discs.

What source drives the high velocity dispersions needed to keep these gas-rich discs stable ($Q \gtrsim 1$) is less clear. Without driving, turbulence decays rapidly on the time-scale of a few times the turbulent crossing time for the disc, $d/\sigma \sim 1\,{\rm kpc}/50\,{\rm km\,s^{-1}} \sim 20\,{\rm Myr}$, where d is the size of the disc (see Elmegreen & Scalo 2004, for a review). Unless the turbulence is sustained by energy injection, Q will drop below unity and the disc will undergo run-away collapse. Gravitational energy from this collapse will be converted to turbulence, but this normally provides only a fraction of the energy required to maintain the observed turbulence for extended periods (Elmegreen & Burkert 2010). Once the gravitational energy has been exhausted and star formation begins, stellar winds and supernova may sustain the necessary turbulence (Mac Low & Klessen 2004; Elmegreen & Burkert 2010).

5.6 The relationship between star formation rate and gas velocity dispersion

We reproduce the result first presented in Green et al. (2010), namely the correlation between the Hα luminosity and velocity dispersion in star-forming galaxies. Fig. 12 shows that the SFR in galaxies with a range of distances (a few Mpc to $z = 3.5$) and stellar masses (10^9 to $10^{11}\,{\rm M}_\odot$) correlates with their gas velocity dispersions. Previously, a dichotomy had been observed between typical gas velocity dispersions of nearby galaxies and those at $z > 1$, but we show there is an empirical relationship between these parameters which connects the two redshift regimes.

Fig. 12 shows several data sets in addition to those reported in Green et al. (2010). Our earlier letter included the samples of Law et al. (2009, 2007b), GHASP (Garrido et al. 2002; Epinat, Amram & Marcelin 2008a; Epinat et al. 2008b), Epinat et al. (2009) and Lemoine-Busserolle et al. (2010). We have added several samples of galaxies at high redshift, including SINS (Cresci et al. 2009), MASSIV (Contini et al. 2012), WiggleZ (Wisnioski et al. 2011) and the samples of Lemoine-Busserolle et al. (2010); Jones et al. (2010) and Swinbank et al. (2012). Notable among these is the sample of Jones et al. (2010), which includes higher spatial resolution data than is typically possible for these redshifts by leveraging gravitational lenses. At intermediate redshift, we include the IMAGES (Yang et al. 2008) survey. In the local Universe, we add the Lyman-break analogues sample of Gonçalves et al. (2010), and local giant H II regions and galaxies from Terlevich & Melnick (1981).

In all cases, the SFR have been corrected for dust extinction and scaled to our adopted Chabrier (2003) IMF. However, the methods used to determine the SFR vary (Hα-luminosity scaling, fits to SEDs, ultraviolet-luminosity scaling) and therefore are not entirely consistent (see Section 5.2). The positions of the DYNAMO galaxies are shown using the beam-smearing-corrected mean velocity dispersion, $\sigma_{m,\,\rm corr}$. For most of the other samples, galaxies are shown using the $\sigma_{\rm m}$ measure of velocity dispersion. Exceptions are the GHASP sample, which uses an unweighted mean; the sample of Epinat et al. (2009), who weight individual velocity dispersions in the average by inverse error; the IMAGES sample, which uses an unweighted mean with the central pixel removed; the SINS survey, which reports velocity dispersions derived from disc modelling and the sample of Terlevich & Melnick (1981), who report an integrated velocity dispersion for an object of comparable or smaller than a single spatial pixel in the other samples. Davies et al. (2011) have shown that the unweighted mean is comparable to the intensity-weighted mean.

The additional samples presented in Fig. 12 all support the correlation (Pearson's $R = 0.72$) between SFR and velocity dispersion in the ionized gas, as previously reported. None of the samples included has been selected in way that would affect the range of velocity dispersions measured. Consequently, we infer galaxies with high dispersion and low SFR or low dispersion and high SFR (corresponding to the empty regions of Fig. 12) must be rare. While no selection bias affects the range in velocity dispersion observed, the ways in which the samples were selected does affect the range of SFR observed. At higher redshifts, only the more luminous highly star-forming galaxies are detected. Also, highly star-forming galaxies are rarer in local samples because of the declining density of global star formation as the Universe ages (Hopkins 2004). These effects that bias the range of SFR observed could combine with the star formation–velocity dispersion relation to create an apparent correlation of velocity dispersion with redshift. Samples that include rarer, higher luminosity nearby galaxies, such as our DYNAMO sample, and those that probe lower luminosity galaxies at higher redshift, such as that of IMAGES or the sub-L_* galaxies of Jones et al., help reject this possibility and confirm the relationship between SFR and velocity dispersion.

The scatter in the correlation is not necessarily unexpected given the varying methods for measuring star formation and velocity dispersion across the various samples shown. Methods for measuring velocity dispersion can be hampered by beam smearing as has already been pointed out, particularly in data of high-redshift galaxies or poorly resolved galaxies. Furthermore, star-formation rates are estimated by a variety of indicators, and dust correction methods also vary. It is especially for these reasons that it would be premature

Downloaded from http://mnras.oxfordjournals.org/ at Liverpool John Moores University on October 27, 2016

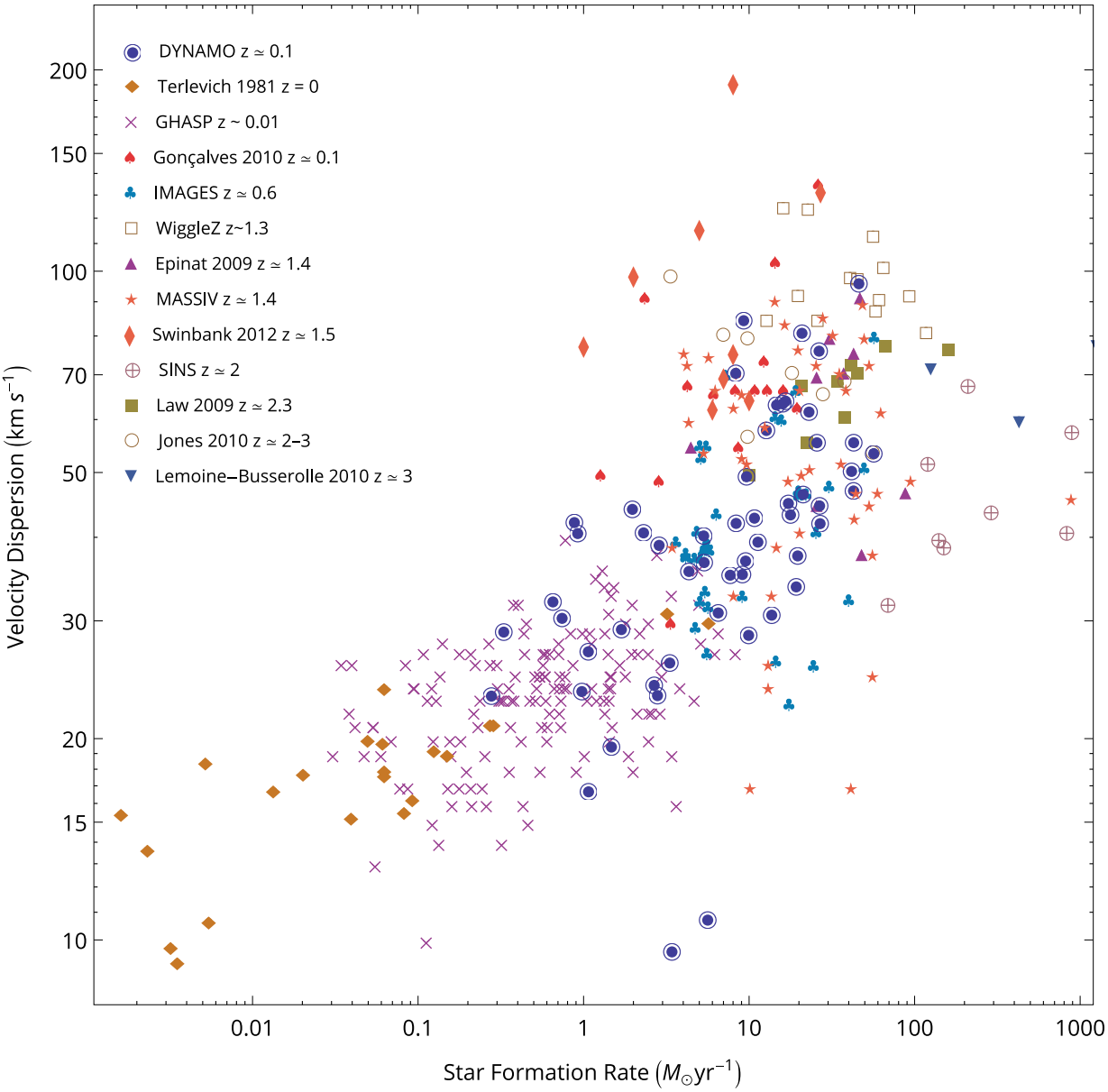

Figure 12. SFR and turbulence are correlated in star-forming objects of all scales and redshifts. Data from a variety of low- and high-redshift galaxies are shown (described in detail in Section 5.6). Also shown are (unresolved) velocity-dispersion measurements of local H II regions. The velocity dispersions do not include large-scale velocity shear (e.g., from disc rotation). Methods for determining SFR vary between samples, and systematic differences in method may account for much of the scatter. A correlation (Pearson's $R = 0.72$) is seen in the data.

to argue for a particular power-law fit until a better understanding of the differences in analysis methods or a self-consistent analysis is available.

Green et al. (2010) also reported that disc-like galaxies with SFR and velocity dispersions comparable to galaxies at $z > 1$ still exist at $z \simeq 0.1$. To confirm that claim, we reproduce Fig. 12, but with DYNAMO galaxies coded by their kinematic classification in Fig. 13. The black points correspond to galaxies from other samples, with larger points corresponding to $z > 1$ galaxies. RD and compact rotating discs (cRD) extend to both high dispersion (even after correction for beam smearing, as measured by $\sigma_{\rm m,corr}$, see Section 4.5) and SFR. Perturbed rotators (PR, cPR) extend to the very highest velocity dispersions. Galaxies classified as RD and PR also follow the TFR, reflecting their disc like nature. The RD and PR classified galaxies show similar SFR and velocity dispersions to those of galaxies above $z > 1$, confirming the claim of our earlier letter. 19 of the 31 galaxies with $\sigma_{\rm m} > 30\,{\rm km\,s^{-1}}$ are classified RD or PR. This correlation supports the idea that turbulence can be sustained by star formation feedback which we discuss further in the next section.

6 DISCUSSION

6.1 Connection between low and high redshift

The sample presented here establishes that a rare but highly star-forming population of galaxies at $z \simeq 0.1$ shows many similar properties to galaxies at $1 < z < 4$. The high gas fractions, gas

Downloaded from http://mnras.oxfordjournals.org/ at Liverpool John Moores University on October 27, 2016

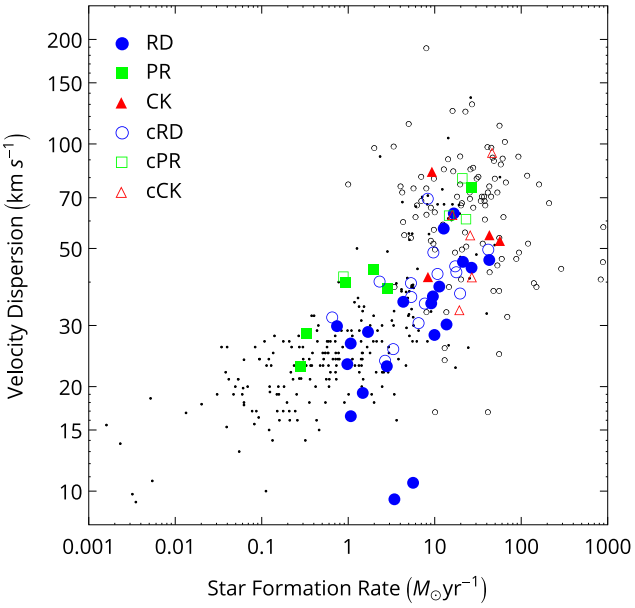

Figure 13. Same as Fig. 12, but with points for our sample of galaxies coded by their kinematic classification (see Section 4.3). Galaxies of other samples with $z < 1$ are shown with black points, and those with $z > 1$ are shown with black circles. The two outliers at the bottom of the figure correspond to galaxies A 4-3 and C 13-3.

velocity dispersions and turbulent RD seen in many integral-field spectroscopic surveys of $z > 1$ galaxies can also be found in our sample at $z \simeq 0.1$ and are not unique to that earlier era of galaxy evolution. Identifying similar galaxies in these two disparate eras provides a link that can be used to improve our understanding of the physical processes of galaxy formation and evolution.

The importance of gas velocity dispersion in star formation and galaxy evolution makes it crucial to compare galaxies from different evolutionary eras. Most local galaxies have ionized gas velocity dispersions of 20–25 km s^{-1} (Andersen et al. 2006; Epinat et al. 2010). These include centre-to-centre dispersions of 5–7 km s^{-1} between H II regions (similar to giant molecular clouds and H I, Stark & Brand 1989); the thermal $10^{4\circ}$K dispersion of the hot H II region gas and the feedback-driven turbulent motions within H II regions (Mezger & Hoglund 1967; Shields 1990). As we have seen, high-redshift galaxies have typical velocity dispersions of 30–90 km s^{-1}. However, we can see in Fig. 12 that our sample and also the local sample of Lyman-break analogues of Gonçalves et al. (2010) overlap with the high-redshift samples and link low- and high-redshift regimes.

The samples also overlap in V/σ values. Most of DYNAMO galaxies with $\sigma_{\rm m} > 40$ km s^{-1} have $1 < V_{2.2R_r}/\sigma_{\rm m} < 8$, which compares with the large discs seen at high-redshift. Gonçalves et al. find $0.5 < V/\sigma < 2$ in their sample, which is more comparable to the 'dispersion-dominated' galaxies at high redshift. Bellocchi et al. (2013) suggest V/σ anticorrelates with infrared luminosity in local galaxies, and may reflect merger stage. In our sample, the discs are dynamically hot but rotation is still dominant. The high inferred gas fractions, up to 70 per cent, are also consistent with measurements at high redshift (Daddi et al. 2010; Tacconi et al. 2010, 2013; Carilli & Walter 2013) and the scaling of V/σ with gas fraction supports the idea of the existence of a gas-rich disc.

The overlap of properties in galaxies from different eras is suggestive of the idea that the same physics is regulating star formation and velocity dispersion at low and high redshift. Physical processes that only operated at high redshift are excluded for our sample. However, these local galaxies having high SFR are rare so one can still allow processes that were common at high redshift but are rare today. These could include processes that are rare in time (for example mergers today) or rare in space (for example regions of the Universe with high cosmic accretion could be rare today). Exactly how rare are DYNAMO galaxies? For $L(\mathrm{H}\alpha) > 10^{42}$ erg s^{-1}, the space density of DYNAMO galaxies is $\sim 10^{-5}$ Mpc^{-3}. These represent 4 per cent of galaxies with masses $>10^{10}$ M$_\odot$ in our redshift range.

Another local sample that is useful for comparison with high redshift is the $z \sim 0.2$ Lyman-break analogues sample, which is similar to our own as a sample of rare galaxies with high SFR. The Lyman-break analogues were selected based on their near-ultraviolet luminosity by Heckman et al. (2005) using the *Galaxy Evolution Explorer* (*GALEX*) space telescope. Their near-ultraviolet luminosity overlaps $2 < z < 3$ Lyman-break galaxies, which are intensely star forming but somewhat lower in stellar mass than near-infrared-selected galaxies at the same redshift (Förster Schreiber et al. 2009). The most compact examples were followed up using AO and integral-field spectroscopy in the Paschen α lines by Basu-Zych et al. (2009) and Gonçalves et al. (2010). The sample observed with integral-field spectroscopy is complementary to our own as shown in Fig. 14. Additionally, the Lyman-break analogues tend to be more compact than DYNAMO galaxies because of their explicit compactness selection criterion. The Lyman-break analogues are more similar in those properties to dispersion-dominated galaxies at high redshift, while our sample is more similar to rotation-dominated galaxies at high redshift. Together, the Lyman-break analogues and DYNAMO samples provide good comparisons with the range of star-forming galaxies seen at high redshift.

6.2 Relationship between turbulence and star formation

The trend between velocity dispersion and star formation indicated by Fig. 12 establishes a relationship for all galaxies with $z < 4$. Instead of an evolution of galaxy velocity dispersions with redshift, we should instead also consider an evolution of galaxies *along* this relation as high SFR galaxies become more common at high redshift. Indications of this relationship have existed for some time in the scaling relations for H II regions (e.g. Terlevich & Melnick 1981; Hippelein 1986; Roy, Arsenault & Joncas 1986; Lehnert et al. 2009, 2013; Wisnioski et al. 2012, to name a few), but only by combining many samples has the relationship, which spans five orders of magnitude in SFR, become clear for galaxies.

The relationship of Fig. 12 may reflect a common mechanism for fuelling star formation in galaxies. In part to explain the turbulent-disc galaxies in the high-redshift Universe, a mechanism whereby cool gas can flow directly on to the galaxy disc has been proposed. In this model, gas is supplied via smooth accretion of cold gas through an unstable hot-gas halo, ('cold flows,' Kereš et al. 2005; Dekel & Birnboim 2006; Dekel et al. 2009). Such cold flows are expected to shut down below redshift $z \simeq 1$ (Crain et al. 2010), and are therefore not expected to be relevant for galaxies in our sample. Brooks et al. (2009) give some evidence that these cold flows may continue for lower mass galaxies beyond $z \simeq 1$, but that cannot explain all of our sample. Gas to fuel the high SFR observed must be delivered in another manner. If there were two different fuelling mechanisms, one for each redshift range, the difference is not manifest in the smooth relationship between star formation and velocity dispersion shown in Fig. 12. The existence of galaxies

Downloaded from http://mnras.oxfordjournals.org/ at Liverpool John Moores University on October 27, 2016

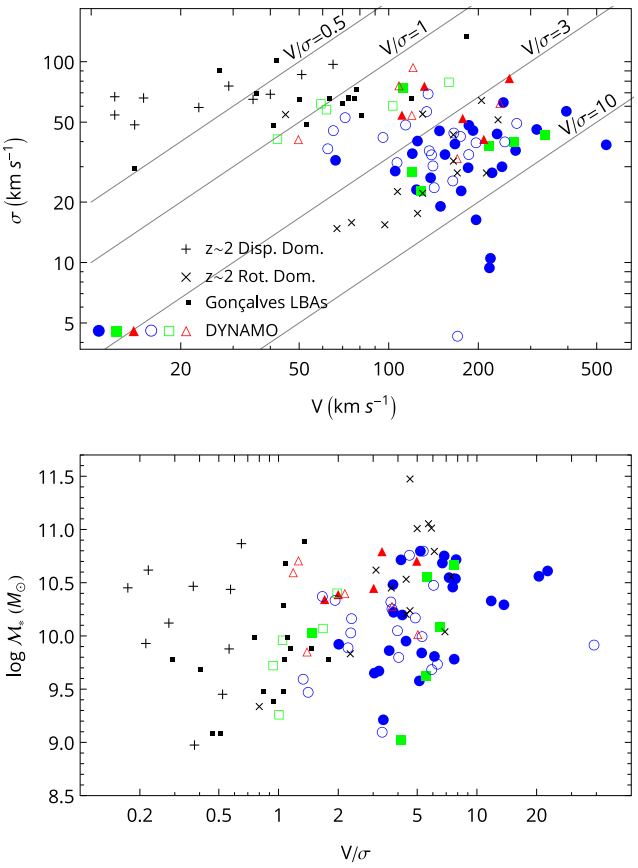

Figure 14. A comparison of our sample and the Lyman-break analogues sample (Gonçalves et al. 2010) and our sample with dispersion-dominated and disc-like galaxies at high redshift. Symbols in both panel are coded the same, and those for DYNAMO galaxies match their kinematic classification as described in Fig. 13. The Lyman-break analogues sample is complementary to DYNAMO: our work probes galaxies with stronger rotation and slightly higher stellar masses – more akin to the SINS disc sample of Cresci et al. (2009) in the properties shown. Lyman-break analogues are more closely matched to the dispersion-dominated sample of Law et al. at high redshift.

with similar properties in both eras suggests that the mechanism may be the same for both populations, or the relationship of Fig. 12 results from physics within the galaxy and is independent of the mechanism of gas supply. We caution though that recent simulations by Nelson et al. (2013) comparing multiple hydrodynamic codes suggests that the delivery of large amounts of cold gas directly into the centres of $z \sim 2$ galaxies may be a numerical artefact, and cold mode accretion may be much less important in building galaxy mass. The distinction between 'hot' and 'cold' modes may not be so clear cut though accretion rates are still higher at high redshift. Observationally, Steidel et al. (2010) see no evidence of filamentary cold flows at $z \sim 2$, but considerable gas falling into galaxy haloes via other mechanisms.

Regardless of how the gas is delivered, once a turbulent, gas-rich disc has formed, the processes governing the conversion of gas into stars should be similar at high and low redshift (except for issues associated with overall gas metallicity). A turbulent disc must be continuously sustained. Two key scenarios are outlined by Genzel et al. (2008); gravitational energy from collapse and feedback from star formation. The first scenario includes energy injection from cosmic accretion (Aumer et al. 2010; Elmegreen & Burkert 2010) but also Toomre disc instabilities, Jeans collapse (Immeli et al. 2004; Aumer et al. 2010; Bournaud et al. 2010; Ceverino et al. 2010) and clump–clump gravitational stirring (Dekel et al. 2009; Ceverino et al. 2010). In the latter scenario, energetic processes associated with star formation, such as stellar winds and supernova, drive turbulence in the gas disc (Lehnert et al. 2009; Le Tiran et al. 2011; Lehnert et al. 2013) as happens in the Milky Way interstellar medium (Mac Low & Klessen 2004; Dib, Bell & Burkert 2006).

Although both of these models probably contribute to the observed velocity dispersion, the relative importance of each is still unclear. Genzel et al. (2008) and Genzel et al. (2011) argue for the importance of gravitational accretion, particularly cold flows, in driving the high velocity dispersions in galaxies of their sample. They quantify the energy in the in-falling gas and suggest a timescale for the dissipation of turbulent energy based on the collision rate of individual large gas clouds. The gas accretion rate evolves cosmologically as the reservoirs of free-floating gas are depleted. Consequently, the energy available to drive turbulence from gravitational accretion declines with time. The accretion rate is further diminished as haloes of hot gas form and block the subsequent infall of cold gas, and as active galactic nuclei form. The decline in accretion rate with time explains why galaxies with high gas velocity dispersions are common early in the history of the Universe, but become rare in the present era. Genzel et al. see very tentative evidence for this decline. However, subsequent analysis by Lehnert et al. (2009, 2013), which is supported by the models of Dekel et al. (2009), suggests that cold flows have insufficient energy to account for the observed turbulence.

Alternatively, feedback processes associated with star formation could drive the observed turbulence, regardless of gas fuelling mechanism. The many processes associated with star formation have long been understood to deliver considerable energy to the interstellar medium, although there is still debate about the relative importance of specific processes. Dib et al. (2006) show how supernova can correlate with turbulence in cool gas using numerical simulations. However, Krumholz & Matzner (2009) argue that supernova may not begin until after the typical star-forming H II region has dispersed. Mac Low & Klessen (2004) review the many sources of mechanical energy from star formation, but are uncertain how efficiently this energy is transferred to the interstellar medium. Förster Schreiber et al. (2009) point out that regardless of the feeding mechanism, high rates of star formation will invariably feed a lot of energy back into the surrounding interstellar medium, leading to high gas turbulence. Our relationship between rates of star formation and gas turbulence, shown in Fig. 12 supports this idea.

Lehnert et al. (2009, 2013); Le Tiran et al. (2011) and Swinbank et al. (2012) also find a relationship between SFR and dispersion, but express it as resolved quantities (i.e. SFR surface density and velocity dispersion per spatial pixel). They argue that an energy input proportional to star formation surface density predicts fairly well the observed velocity dispersion. Numerical estimates of the mechanical energy from star formation also match the energy requirement to maintain the turbulence observed in the Lehnert et al. (2009, 2013) galaxy sample. Therefore, energy feedback from star formation processes alone could drive the observed turbulence in galaxies at all redshifts. However, Lehnert et al. (2009, 2013) in particular see a lot of galaxy-to-galaxy variation in their sample. Their data were for natural seeing with only 5–8 kpc resolution, making it difficult to disentangle resolved quantities from global ones. In our own data, we see only a weak correlation at best in spaxel-to-spaxel data, although the much larger errors would weaken any correlation. Genzel et al. (2011) consider this issue with AO data

Downloaded from http://mnras.oxfordjournals.org/ at Liverpool John Moores University on October 27, 2016

on high-redshift galaxies and fail to see a correlation on smaller (sub-galactic) scales.

Turbulence at high-redshift is most likely sustained by multiple mechanisms. For example, Elmegreen & Burkert (2010) explore a model where gravitational accretion energy sets the initial structure in primordial galaxies before star formation begins. Then, once widespread star formation starts, the associated feedback of energy controls the later evolution of the galaxy. In this model, the initial accretion of gas leads to very high velocity dispersions, such that galaxy-size clouds of gas remain Toomre- and Jeans-stable against star formation. As this initial energy dissipates, the cloud fragments into large star-forming complexes, where energy from star formation then controls the subsequent evolution of the turbulence. Such a combination of drivers for turbulence is much more likely than any one process remaining universally dominant, and this picture certainly fits well with both existing observations and simulations, but is not yet proven.

7 CONCLUSIONS

We have observed, using integral-field spectroscopy, a sample of 67 galaxies covering a range in Hα luminosities selected from the SDSS. The selection has been structured to ensure that a large fraction of the galaxies observed are rare, highly Hα-luminous galaxies, which would be most easily detected with integral-field spectroscopy were they at $z \gtrsim 2$. Analysis of this galaxy sample has led to the following conclusions.

(i) Narrow-band images of our galaxies centred on the Hα emission line show a range in morphologies. Most of the sample are centrally concentrated, but some show two distinct concentrations or several smaller knots of decentralized star formation.

(ii) The majority of the sample show indications of disc-like rotation using common qualitative classification criteria. The confirmed disc galaxies show a reasonable agreement with the TFR.

(iii) Galaxies in our sample with SFR greater than a few $M_\odot\ yr^{-1}$ often show high (greater than 40 km s^{-1}) velocity dispersions in the ionized gas component. This subset also overlaps with typical SFR and velocity dispersions of high-redshift samples observed with integral-field spectroscopy.

(iv) We find V/σ values similar to high-redshift discs, they are greater than 'dispersion-dominated galaxies' (both at low and high redshift) but much less than modern large spiral galaxies.

(v) The range in stellar masses for galaxies in our sample overlaps with the range covered by rotation-dominated galaxies at high redshift.

(vi) The same highly star-forming portion of our sample is also expected to be gas rich, with inferred gas fractions as high as 70 per cent. The median gas fraction of 41 per cent is still much higher than typical local gas fractions in star-forming galaxies of ∼10 per cent (Saintonge et al. 2011). Gas fraction correlates only weakly, if at all, with stellar mass, SFR and velocity dispersion in our sample. However, we do see a good correlation with V/σ in the manner predicted for marginally stable gas-rich Toomre discs.

(vii) The gas velocity dispersion in galaxies correlates with their SFR. This correlation holds across a broad range of samples and redshifts. Beam smearing due to disc rotation, which can affect the measure of the velocity dispersion, does not affect this result in our sample.

(viii) Some highly star-forming galaxies show inferred gas fractions, velocity dispersions, kinematic morphologies and SFR similar to samples of galaxies at high redshift. Furthermore, study of the sample presented here can inform understanding of star formation in high-redshift galaxies.

7.1 Future work

The sample of galaxies we have defined here, while diverse, overlaps in many properties with typical galaxies at high redshift. If they are true analogues then their proximity will allow a great range of detailed study of astrophysical processes in such objects. For example, they can be studied at greater spatial resolution (via AO) and across multiple wavelengths not possible at high redshift.

In this first paper of the series, we make a prediction which we will test throughout the series. We predict that there is no evolution between $z \sim 0.1$ and $z \sim 2$ in the nature of star formation or the fuelling mechanisms of star-forming galaxies. Instead, the 'evolution' in star formation and relative fractions of galaxy types across that time we predict is a result of the reduction in the available gas and buildup of cosmological structure. Here, and in Green et al. (2010), we already have tentative evidence that both the kinematics and gas supplies remain similar for galaxies of similar SFR in these two eras.

In future papers in this series we will consider the following.

(i) High-resolution morphology both from ground-based imaging using AO and space-based Hubble imaging. Do we see kpc-sized clumps of star formation (Elmegreen et al. 2005), similar to high-redshift galaxies, as predicted by the Jeans instability scenario?

(ii) Can we confirm the high-gas fractions using molecular gas observations, for example using the CO line?

(iii) How does the Star Formation Law linking gas and SFR surface densities compare with more normal galaxies and with high redshift? What role does velocity dispersion play in self-regulation?

(iv) Can we detect thermal dust emission from far-infrared observations and relate the dust–mass and luminosity to those of classical LIRGs and ULIRGs?

(v) Can we measure the *stellar kinematics* with deep resolved absorption-line spectra and confirm the ionized gas really is tracing a young stellar disc? Does the high dispersions correspond to young, *thick* stellar discs?

(vi) How do resolved quantities, such as metallicity, in local galaxies compare with high-redshift discs? For example, there has been some evidence for *positive* metallicity gradients in some samples (Toomre 1964; Cresci et al. 2010; Queyrel et al. 2012) interpreted as arising from cold flows.

We live in an exciting time in the study of galaxy assembly. The use of AO and integral-field spectroscopy have revolutionized our pictures of galaxy assembly. In the next few years, the advent of powerful new facilities such as Atacama Large Millimeter/submillimeter Array (ALMA) and the next generation of large optical telescopes will allow cold gas and stellar motions at low and high redshift to be measured directly and allow questions raised by the low- and high-redshift samples to be answered.

ACKNOWLEDGEMENTS

In addition to the named authors who have contributed to this paper, we thank additional DYNAMO team members Danail Obreschkow, Attila Popping, Matthew Satterthwaite, Rob Bassett, Erin Mentuch-Cooper and David Fisher who read and commented on this manuscript.

We thank the staff of the Australian Astronomical Observatory and the Australian National University's 2.3 m telescope for

Downloaded from http://mnras.oxfordjournals.org/ at Liverpool John Moores University on October 27, 2016

supporting the observations presented here. Finally, we appreciate the referees time, comments and suggestions, which improved this manuscript.

REFERENCES

Abraham R. G., van den Bergh S., Glazebrook K., Ellis R. S., Santiago B. X., Surma P., Griffiths R. E., 1996a, ApJS, 107, 1
Abraham R. G., Tanvir N. R., Santiago B. X., Ellis R. S., Glazebrook K., van den Bergh S., 1996b, MNRAS, 279, L47
Adelman-McCarthy J. K. et al., 2006, ApJS, 162, 38
Andersen D. R., Bershady M. A., Sparke L. S., Gallagher J. S., III, Wilcots E. M., van Driel W., Monnier-Ragaigne D., 2006, ApJS, 166, 505
Argence B., Lamareille F., 2009, A&A, 495, 759
Arribas S., Colina L., Monreal-Ibero A., Alfonso J., García-Marín M., Alonso-Herrero A., 2008, A&A, 479, 687
Arribas S., Colina L., Alonso-Herrero A., Rosales-Ortega F. F., Monreal-Ibero A., García-Marín M., García-Burillo S., Rodríguez-Zaurín J., 2012, A&A, 541, A20
Aumer M., Burkert A., Johansson P. H., Genzel R., 2010, ApJ, 719, 1230
Baldry I. K., Glazebrook K., Brinkmann J., Ivezić Ž., Lupton R. H., Nichol R. C., Szalay A. S., 2004, ApJ, 600, 681
Baldry I. K., Balogh M. L., Bower R. G., Glazebrook K., Nichol R. C., Bamford S. P., Budavari T., 2006, MNRAS, 373, 469
Baldwin J. A., Phillips M. M., Terlevich R., 1981, PASP, 93, 5
Basu-Zych A. R. et al., 2009, ApJ, 699, L118
Baugh C. M., Cole S., Frenk C. S., 1996, MNRAS, 282, L27
Begeman K. G., 1989, A&A, 223, 47
Bell E. F., de Jong R. S., 2001, ApJ, 550, 212
Bellocchi E., Arribas S., Colina L., 2012, A&A, 542, A54
Bellocchi E., Arribas S., Colina L., Miralles-Caballero D., 2013, A&A, 557, A59
Bell E. F. et al., 2005, ApJ, 625, 23
Bershady M. A., Verheijen M. A. W., Swaters R. A., Andersen D. R., Westfall K. B., Martinsson T., 2010, ApJ, 716, 198
Bournaud F., Elmegreen B. G., Martig M., 2009, ApJ, 707, L1
Bournaud F., Elmegreen B. G., Teyssier R., Block D. L., Puerari I., 2010, MNRAS, 409, 1088
Brinchmann J., Charlot S., White S. D. M., Tremonti C., Kauffmann G., Heckman T., Brinkmann J., 2004, MNRAS, 351, 1151
Brooks A. M., Governato F., Quinn T., Brook C. B., Wadsley J., 2009, ApJ, 694, 396
Calzetti D., 1997, AJ, 113, 162
Calzetti D., Kinney A. L., Storchi-Bergmann T., 1996, ApJ, 458, 132
Cappellari M. et al., 2011, MNRAS, 413, 813
Carilli C., Walter F., 2013, ARA&A, 51, 105
Ceverino D., Dekel A., Bournaud F., 2010, MNRAS, 404, 2151
Chabrier G., 2003, PASP, 115, 763
Chiu K., Bamford S. P., Bunker A., 2007, MNRAS, 377, 806
Cole S., Lacey C. G., Baugh C. M., Frenk C. S., 2000, MNRAS, 319, 168
Colina L., Arribas S., Monreal-Ibero A., 2005, ApJ, 621, 725
Conselice C. J., 2003, ApJS, 147, 1
Contini T. et al., 2012, A&A, 539, A91
Courteau S., 1997, AJ, 114, 2402
Covington M. D. et al., 2010, ApJ, 710, 279
Crain R. A., McCarthy I. G., Frenk C. S., Theuns T., Schaye J., 2010, MNRAS, 407, 1403
Cresci G., Mannucci F., Maiolino R., Marconi A., Gnerucci A., Magrini L., 2010, Natureure, 467, 811
Cresci G. et al., 2009, ApJ, 697, 115
Daddi E. et al., 2007, ApJ, 670, 156
Daddi E. et al., 2010, ApJ, 713, 686
Davies R., Kasper M., 2012, ARA&A, 50, 305
Davies R. et al., 2011, ApJ, 741, 69
Dekel A., Birnboim Y., 2006, MNRAS, 368, 2
Dekel A., Sari R., Ceverino D., 2009, ApJ, 703, 785
Dekel A. et al., 2009, Nat, 457, 451
Dib S., Bell E., Burkert A., 2006, ApJ, 638, 797
Dopita M., Hart J., McGregor P., Oates P., Bloxham G., Jones D., 2007, Ap&SS, 310, 255
Dopita M. et al., 2010, Ap&SS, 327, 245
Elmegreen B. G., Burkert A., 2010, ApJ, 712, 294
Elmegreen B. G., Elmegreen D. M., 2005, ApJ, 627, 632
Elmegreen B. G., Elmegreen D. M., 2006, ApJ, 650, 644
Elmegreen B. G., Scalo J., 2004, ARA&A, 42, 211
Elmegreen D. M., Elmegreen B. G., Hirst A. C., 2004, ApJ, 604, L21
Elmegreen D. M., Elmegreen B. G., Rubin D. S., Schaffer M. A., 2005, ApJ, 631, 85
Elmegreen D. M., Elmegreen B. G., Marcus M. T., Shahinyan K., Yau A., Petersen M., 2009, ApJ, 701, 306
Epinat B., Amram P., Marcelin M., 2008a, MNRAS, 390, 466
Epinat B. et al., 2008b, MNRAS, 388, 500
Epinat B. et al., 2009, A&A, 504, 789
Epinat B., Amram P., Balkowski C., Marcelin M., 2010, MNRAS, 401, 2113
Epinat B. et al., 2012, A&A, 539, A92
Erb D. K., Steidel C. C., Shapley A. E., Pettini M., Reddy N. A., Adelberger K. L., 2006a, ApJ, 646, 107
Erb D. K., Steidel C. C., Shapley A. E., Pettini M., Reddy N. A., Adelberger K. L., 2006b, ApJ, 647, 128
Flores H., Hammer F., Puech M., Amram P., Balkowski C., 2006, A&A, 455, 107
Förster Schreiber N. M. et al., 2006, ApJ, 645, 1062
Förster Schreiber N. M. et al., 2009, ApJ, 706, 1364
Freeman K. C., 1970, ApJ, 160, 811
Garrido O., Marcelin M., Amram P., Boulesteix J., 2002, A&A, 387, 821
Genzel R. et al., 2006, Nat, 442, 786
Genzel R. et al., 2008, ApJ, 687, 59
Genzel R. et al., 2011, ApJ, 733, 101
Glazebrook K., 2013, preprint (arXiv:e-prints)
Gnerucci A. et al., 2011, A&A, 528, A88
Gonçalves T. S. et al., 2010, ApJ, 724, 1373
Green A. W. et al., 2010, Nat, 467, 684
Hammer F., Puech M., Chemin L., Flores H., Lehnert M. D., 2007, ApJ, 662, 322
Heckman T. M. et al., 2005, ApJ, 619, L35
Hippelein H. H., 1986, A&A, 160, 374
Hodge J. A., Carilli C. L., Walter F., de Blok W. J. G., Riechers D., Daddi E., Lentati L., 2012, ApJ, 760, 11
Hopkins A. M., 2004, ApJ, 615, 209
Hopkins A. M., Beacom J. F., 2006, ApJ, 651, 142
Immeli A., Samland M., Westera P., Gerhard O., 2004, ApJ, 611, 20
Jones T. A., Swinbank A. M., Ellis R. S., Richard J., Stark D. P., 2010, MNRAS, 404, 1247
Juneau S. et al., 2005, ApJ, 619, L135
Kassin S. A. et al., 2007, ApJ, 660, L35
Kassin S. A. et al., 2012, ApJ, 758, 106
Kauffmann G. et al., 2003a, MNRAS, 341, 33
Kauffmann G. et al., 2003b, MNRAS, 346, 1055
Kennicutt R. C., Jr, 1998a, ARA&A, 36, 189
Kennicutt R. C., Jr, 1998b, ApJ, 498, 541
Kereš D., Katz N., Weinberg D. H., Davé R., 2005, MNRAS, 363, 2
Kroupa P., 2001, MNRAS, 322, 231
Krumholz M. R., Matzner C. D., 2009, ApJ, 703, 1352
Krumholz M. R., Dekel A., McKee C. F., 2012, ApJ, 745, 69
Law D. R., Steidel C. C., Erb D. K., Pettini M., Reddy N. A., Shapley A. E., Adelberger K. L., Simenc D. J., 2007a, ApJ, 656, 1
Law D. R., Steidel C. C., Erb D. K., Larkin J. E., Pettini M., Shapley A. E., Wright S. A., 2007b, ApJ, 669, 929
Law D. R., Steidel C. C., Erb D. K., Larkin J. E., Pettini M., Shapley A. E., Wright S. A., 2009, ApJ, 697, 2057
Le Tiran L., Lehnert M. D., van Driel W., Nesvadba N. P. H., Di Matteo P., 2011, A&A, 534, L4
Lehnert M. D., Nesvadba N. P. H., Tiran L. L., Matteo P. D., van Driel W., Douglas L. S., Chemin L., Bournaud F., 2009, ApJ, 699, 1660

Downloaded from http://mnras.oxfordjournals.org/ at Liverpool John Moores University on October 27, 2016

Lehnert M. D., Le Tiran L., Nesvadba N. P. H., van Driel W., Boulanger F., Di Matteo P., 2013, A&A, 555, A72
Lemoine-Busserolle M., Lamareille F., 2010, MNRAS, 402, 2291
Lemoine-Busserolle M., Bunker A., Lamareille F., Kissler-Patig M., 2010, MNRAS, 401, 1657
Mac Low M., Klessen R. S., 2004, Rev. Mod. Phys., 76, 125
Madau P., Ferguson H. C., Dickinson M. E., Giavalisco M., Steidel C. C., Fruchter A., 1996, MNRAS, 283, 1388
Markwardt C. B., 2009, in Bohlender D. A., Durand D., Dowler P., eds, ASP Conf. Ser. Vol. 411, Astronomical Data Analysis Software and Systems XVIII. Astron. Soc. Pac., San Francisco, p. 251
Mathewson D. S., Ford V. L., 1996, ApJS, 107, 97
McGaugh S. S., 2005, ApJ, 632, 859
McGaugh S. S., Schombert J. M., Bothun G. D., de Blok W. J. G., 2000, ApJ, 533, L99
Mezger P. G., Hoglund B., 1967, ApJ, 147, 490
Miller S. H., Bundy K., Sullivan M., Ellis R. S., Treu T., 2011, ApJ, 741, 115
Miller S. H., Ellis R. S., Sullivan M., Bundy K., Newman A. B., Treu T., 2012, ApJ, 753, 74
Nelson D., Vogelsberger M., Genel S., Sijacki D., Kereš D., Springel V., Hernquist L., 2013, MNRAS, 429, 3353
Nesvadba N. P. H. et al., 2006, ApJ, 650, 661
Nesvadba N. P. H. et al., 2007, ApJ, 657, 725
Newman S. F. et al., 2013, ApJ, 767, 104
Noeske K. G. et al., 2007, ApJ, 660, L43
Noguchi M., 1998, Nat, 392, 253
Pizagno J. et al., 2005, ApJ, 633, 844
Pizagno J. et al., 2007, AJ, 134, 945
Puech M. et al., 2008, A&A, 484, 173
Puech M., Hammer F., Flores H., Delgado-Serrano R., Rodrigues M., Yang Y., 2010, A&A, 510, A68
Queyrel J. et al., 2012, A&A, 539, A93
Roy J., Arsenault R., Joncas G., 1986, ApJ, 300, 624
Saintonge A. et al., 2011, MNRAS, 415, 32
Sánchez S. F. et al., 2012, A&A, 538, A8
Shapiro K. L. et al., 2008, ApJ, 682, 231
Sharp R. et al., 2006, in McLean I. S., Iye M., Proc. SPIE Conf. Ser., Vol. 6269, Ground-based and Airborne Instrumentation for Astronomy. SPIE, Bellingham, p. 62690G
Shields G. A., 1990, ARA&A, 28, 525
Stark A. A., Brand J., 1989, ApJ, 339, 763
Stark D. P., Swinbank A. M., Ellis R. S., Dye S., Smail I. R., Richard J., 2008, Nat, 455, 775
Steidel C. C., Giavalisco M., Pettini M., Dickinson M., Adelberger K. L., 1996, ApJ, 462, L17
Steidel C. C., Erb D. K., Shapley A. E., Pettini M., Reddy N., Bogosavljević M., Rudie G. C., Rakic O., 2010, ApJ, 717, 289
Strauss M. A. et al., 2002, AJ, 124, 1810
Swinbank A. M., Bower R. G., Smith G. P., Wilman R. J., Smail I., Ellis R. S., Morris S. L., Kneib J. P., 2007, MNRAS, 376, 479
Swinbank A. M. et al., 2009, MNRAS, 400, 1121
Swinbank A. M. et al., 2011, ApJ, 742, 11
Swinbank A. M., Smail I., Sobral D., Theuns T., Best P. N., Geach J. E., 2012, ApJ, 760, 130
Tacconi L. J. et al., 2010, Nat, 463, 781
Tacconi L. J. et al., 2013, ApJ, 768, 74
Terlevich R., Melnick J., 1981, MNRAS, 195, 839
Tody D., 1993, in Hanisch R. J., Brissenden R. J. V., Barnes J., eds, ASP Conf. Ser. Vol. 52, Astronomical Data Analysis Software and Systems II. Astron. Soc. Pac., San Francisco, p. 173
Toomre A., 1964, ApJ, 139, 1217
Tremonti C. A. et al., 2004, ApJ, 613, 898
Tully R. B., Fisher J. R., 1977, A&A, 54, 661
van den Bergh S., Abraham R. G., Ellis R. S., Tanvir N. R., Santiago B. X., Glazebrook K. G., 1996, AJ, 112, 359
Vergani D. et al., 2012, A&A, 546, A118
Verheijen M. A. W., 2001, ApJ, 563, 694
Westmoquette M. S., Clements D. L., Bendo G. J., Khan S. A., 2012, MNRAS, 424, 416
Wisnioski E. et al., 2011, MNRAS, 417, 2601
Wisnioski E., Glazebrook K., Blake C., Poole G. B., Green A. W., Wyder T., Martin C., 2012, MNRAS, 422, 3339
Wright S. A. et al., 2007, ApJ, 658, 78
Wright S. A., Larkin J. E., Law D. R., Steidel C. C., Shapley A. E., Erb D. K., 2009, ApJ, 699, 421
Yang Y. et al., 2008, A&A, 477, 789
York D. G. et al., 2000, AJ, 120, 1579
Yuan T. T., Kewley L. J., Swinbank A. M., Richard J., Livermore R. C., 2011, ApJ, 732, L14
Yuan T. T., Kewley L. J., Swinbank A. M., Richard J., 2012, ApJ, 759, 66

APPENDIX A: REMOVING THE EFFECTS OF BEAM SMEARING FROM DISPERSION MAPS OF ROTATING DISC GALAXIES

Here, we present an approach to compute and remove the effects of beam smearing from velocity-dispersion maps obtained from integral-field spectroscopy. The method presented below fully accounts for any additional dispersion arising from unresolved velocity gradient across the sampling resolution.

Beam smearing describes the smearing of a velocity gradient perpendicular to the line of sight into increased velocity dispersion along the line of sight. Spatial pixel of an integral-field spectrograph covers a finite part of the galaxy, and any velocity gradient across that area will be detected only as increased velocity dispersion. Therefore, this effect can bias spatially resolved velocity-dispersion measurements, particularly near the steep inner rotation curve found in most RD galaxies (Davies et al. 2011).

When the intrinsic velocity field is known, the velocity profile for each spatial sample can be computed exactly, and then removed from observations before computing the spatially resolved velocity dispersion. The computation for a simple RD with an arctangent-like rotation curve is presented here.

We begin by defining a functional form to the iso-velocity contours in the observed plane of the galaxy. In polar coordinates, we can write the observed velocity at every point as a function of the rotation curve, $V(r)$, inclination, i, and position angle on the sky, ϕ,

$$V_{\rm obs}(r, \phi) = V(r) \sin i \cos \phi. \tag{A1}$$

For the velocity curve, we adopt that of our disc model,

$$V(r) = V_{\rm circ} \frac{2}{\pi} \arctan(r/r_t). \tag{A2}$$

We can then compute the path of an iso-velocity contour by setting this function equal to a particular velocity, $V_{\rm obs} = v$, and solve to find

$$r_{\rm iso}(v, \phi) = r_t \tan\left(\frac{\pi v \csc i \sec \phi}{2V_{\rm circ}}\right). \tag{A3}$$

Next, we assume that the projected intensity of the light associated with this rotation is that of an exponential disc, $I(r) = I_0 \exp r/h$. For our purposes, the overall normalization I_0 is irrelevant, so we set it to 1. The exponential scale radius of the galaxy is h. We can then project this intrinsic intensity distribution to the observed plane, giving

$$I(r, \phi) = \exp\left(\frac{r\sqrt{(\cos\phi \sin i)^2 + (\sin\phi)^2}}{h}\right). \tag{A4}$$

Downloaded from http://mnras.oxfordjournals.org/ at Liverpool John Moores University on October 27, 2016

We can then recover the integrated velocity profile, $f(V)$, (i.e. the integrated spectrum) by conducting a line integral of I along each iso-velocity contour:

$$f(V) = \oint_V I \, \mathrm{d}s. \tag{A5}$$

The length element is given by

$$\mathrm{d}s = \sqrt{r_{\rm iso}^2 + \left(\frac{d}{\mathrm{d}\phi} r_{\rm iso}\right)^2} \, \mathrm{d}\phi \tag{A6}$$

which allows us to write the line integral as a normal integral,

$$f(V) = \int_\phi I \sqrt{r_{\rm iso}^2 + \left(\frac{d}{\mathrm{d}\phi} r_{\rm iso}\right)^2} \, \mathrm{d}\phi \tag{A7}$$

The limits of integration are given by the limits of the line, which are the solutions to

$$r_{\rm iso}(v, \phi) = \pm\pi/2. \tag{A8}$$

With this formalism, we can generate the observed, integrated velocity spectrum for the whole galaxy with $f(V)$. Furthermore, by introducing a window function on the intensity, we can recover the velocity spectrum for any sub region of the galaxy. For a square pixel, this window function is constructed of several Heaviside (unit) step functions in rectangular coordinates:

$$W(x, y) = H(x + x_{\rm min}) H(y + y_{\rm min}) H(1 - x + x_{\rm min}) \times H(1 - y + x_{\rm min}), \tag{A9}$$

where we have set the size of the pixel to one, and the position of the lower left corner of the pixel is given by $(x_{\rm min}, y_{\rm min})$. This window can then be convolved with a Gaussian seeing function with FWHM of s to give:

$$W_{\rm seeing} = \frac{1}{4} \left[\mathrm{erf}\left(\frac{x - x_{\rm min} - 1}{\sqrt{2}s}\right) - \mathrm{erf}\left(\frac{x + x_{\rm min}}{\sqrt{2}s}\right) \right] \times \left[\mathrm{erf}\left(\frac{y - y_{\rm min} - 1}{\sqrt{2}s}\right) - \mathrm{erf}\left(\frac{y - y_{\rm min}}{\sqrt{2}s}\right) \right]. \tag{A10}$$

We can then write the velocity spectrum for an individual pixel, $f_{\rm pix}(V)$ (including 'beam smearing', i.e. seeing) as

$$f_{\rm pix}(V) = \oint_V I W_{\rm seeing} \mathrm{d}s. \tag{A11}$$

This allows us to compute the spectrum due to beam smearing of the velocity map within each spatial pixel. The beam smearing velocity width can then be subtracted (in quadrature) from the observed velocity dispersion in each pixel to recover a spatially resolved map of velocity dispersion which is free of beam smearing arising from the differential rotation of the disc. In the rare cases, where the beam smearing correction is larger than the observed velocity dispersion, we set the velocity dispersion to zero. Thus, these spaniels do not contribute to the final $\sigma_{\rm m}$.

SUPPORTING INFORMATION

Additional Supporting Information may be found in the online version of this article:

Figure 15. SDSS three colour (gri) image, and spatially resolved properties for all our objects. The SDSS image shows an overlay of the field of view of the integral-field spectrograph, and corresponds to the edges of the subsequent maps (http://mnras.oxfordjournals.org/lookup/suppl/doi:10.1093/mnras/stt1882/-/DC1).

Please note: Oxford University Press are not responsible for the content or functionality of any supporting materials supplied by the authors. Any queries (other than missing material) should be directed to the corresponding author for the article.

This paper has been typeset from a TEX/LATEX file prepared by the author.

Downloaded from http://mnras.oxfordjournals.org/ at Liverpool John Moores University on October 27, 2016